Ore Geology Reviews 39 (2011) 188–217

Contents lists available at ScienceDirect

Ore Geology Reviews

journal homepage: www.elsevier.com/locate/oregeorev

Trace and minor elements in sphalerite from base metal deposits in South China: A LA-ICPMS study

Lin Ye [a,*], Nigel J. Cook [b,c], Cristiana L. Ciobanu [b], Liu Yuping [a], Zhang Qian [a], Liu Tiegeng [a], Gao Wei [a,d], Yang Yulong [a,d], Leonid Danyushevskiy [e]

[a] State Key Laboratory of Ore Deposit Geochemistry, Institute of Geochemistry, Chinese Academy of Sciences, Guiyang 550002, China
[b] Centre for Tectonics, Resources and Exploration (TRaX), School of Earth and Environmental, Sciences, University of Adelaide, SA 5005, Australia
[c] South Australian Museum, Adelaide, SA, Australia
[d] Graduate School of Chinese Academy of Sciences, Beijing, 100049, China
[e] CODES, University of Tasmania, Hobart, Tas., Australia

ARTICLE INFO

Article history:
Received 8 November 2010
Received in revised form 4 March 2011
Accepted 4 March 2011
Available online 11 March 2011

Keywords:
Sphalerite
Mineral chemistry
LA-ICPMS trace element analysis
Indium
South China

ABSTRACT

Laser-ablation ICP mass-spectroscopy has been used to investigate the geochemistry of sphalerite in a range of nine Zn–Pb deposits in South China. The deposits, which are of different ages and belong to different metallogenic provinces, have been assigned to the following genetic types: skarn (Hetaoping, Luziyuan), syngenetic massive sulphide (Dabaoshan, Laochang and Bainiuchang) and Mississippi-Valley-type (Huize, Mengxing, Niujiaotang) based on the features of the ore, even though their origin is heavily debated based on other criteria. The giant Jinding deposit is considered separately. Sphalerite from each genetic class of deposit shows a distinct chemical signature. Sphalerite from the skarn deposits is characterised by elevated, lattice-bound concentrations of Co and Mn. The distal character of these skarn systems is reflected by the low In content of sphalerite. The three syngenetic massive sulphide deposits feature sphalerite strongly enriched in In, Sn and Ga, whereas the deposits of MVT-type are typically enriched in Ge, Cd, Tl and As. These divergent characters are reflected in absolute element abundances as well as in element ratios.

Time-resolved depth profiles for sphalerite from the Chinese deposits confirm the presence of elements such as Co, In, Ge, Ga, and Cd in solid solution, but the dataset expands the understanding of sphalerite mineral chemistry by also indicating that other elements, whose ability to enter the crystal structure of sphalerite has been previously debated (Ag, Sn, Tl, Sb), may also be in solid solution.

Sphalerite is a refractory mineral and trace element analysis of sphalerite shows promise as a tracer of ore genesis even in overprinted ores. Systematic work on larger sample suites may help define the geochemical signature of different metallogenic epochs in regions as geologically complex as South China and help resolve the mechanism by which many of the debated ore deposits were formed.

1. Introduction

Sphalerite is one of the most common sulphide minerals and by far the economically most abundant source of zinc. The crystal structure of sphalerite has long been recognised to accommodate a broad variety of elements, the most significant of which are Fe and Cd. Many elements enter the sphalerite structure via simple substitution of similar-sized ions ($Zn^{2+} \leftrightarrow Fe^{2+}$, Cd^{2+}, Mn^{2+}, Co^{2+} or $S^{2-} \leftrightarrow Se^{2-}$), or by coupled substitution (e.g., $Zn^{2+} \leftrightarrow Cu^{+} + In^{3+}$). Substitution mechanisms for other elements commonly found in sphalerite (e.g. Sn, Ag, Ga, and Ge) remain less well constrained and for others (e.g., Pb, Tl, As, Sb, and Bi), it is not entirely clear whether they enter the sphalerite structure at all or are almost always present as inclusions of discrete minerals. The reader is referred to the sizeable literature on the minor and trace element geochemistry of sphalerite, including-Fleischer (1955), Zhang (1987), Johan (1988), Huston et al. (1995), Beaudoin (2000), Di Benedetto et al. (2005), Ishihara et al. (2006), Ishihara and Endo (2007) and Cook et al. (2009).

It is only relatively recently, however, that widely available, relatively inexpensive, precise analytical methods have been applied to document and correlate trace element distributions in sphalerite from a large number of ore deposits. Such work has confirmed arguments first put forward more than 70 years ago (Oftedahl, 1940) that the trace element endowment of sphalerite can, to a large extent, be correlated with genetic type. Thus, sphalerite from SEDEX-style massive sulphide deposits can be expected to show a different signature from sphalerite in proximal skarns, epithermal vein deposits or Mississippi-Valley-type (MVT) ores (Cook et al., 2009 and references therein).

* Corresponding author. Tel.: +86 8515895591.
E-mail address: yelin@vip.gyig.ac.cn (L. Ye).

0169-1368/$ – see front matter © 2011 Elsevier B.V. All rights reserved.
doi:10.1016/j.oregeorev.2011.03.001

The purpose of the present contribution is two-fold. Firstly, we expand the dataset for sphalerite described by Cook et al. (2009), using near-identical methodology in the same laboratory to gain a greater understanding of the range of trace elements in natural sphalerite. Secondly, we test the usefulness of sphalerite mineral chemistry to discriminate genetic type. To achieve this, we have analysed sphalerite from nine Zn–Pb and polymetallic ores from South China. Each of the selected deposits has been assigned to a specific genetic type based on overall macroscale features, prevailing ore textures and our evaluation of evidence presented in the literature. There exists, however, substantial debate about the origin of most, if not all, of the deposits we have selected, with a wide variety of alternative explanations presented in both the Chinese and international literature. These controversies are amplified by the geological complexity of South China.

2. Regional geology and geodynamic evolution

South China hosts many thousands of base metal deposits and smaller occurrences; some of these are world class giants, e.g., Jinding. They vary in deposit style from skarn and Mississippi-Valley-type (MVT) to stratabound and/or stratiform massive sulphides, the latter including volcanic-hosted (VMS), sedimentary exhalative (SEDEX) and sediment-hosted ores. The deposits under consideration are

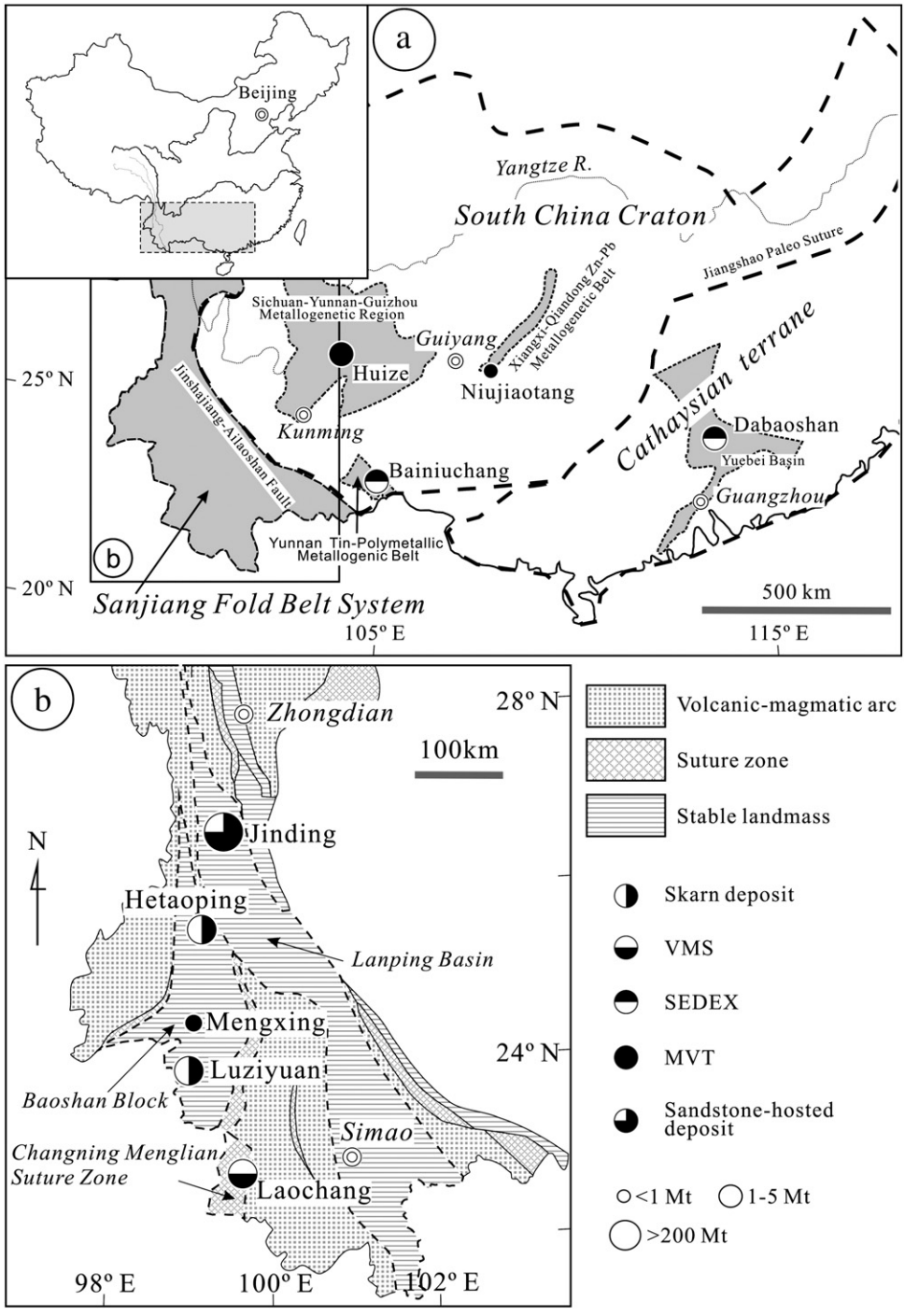

Fig. 1. (a) Geological sketch map of South China showing the location and tectonic setting of the deposits studied. The inset (b) is an enlargement of the Sanjiang Fold Belt. Maps are redrawn after Wang (1993), Zhou et al. (1998), C.Q. Zhang et al., 2005b; Hou et al. (2007) and Pan et al. (2009).

Table 1
Geological features of the ore deposits in Southern China from which sphalerite have been studied.

Deposit/type	Province/ tectonic unit	Ore tonnage (Mt)	Grade (wt.%)				By-product commodities	Orebody morphology	Host lithology	Mineralisation age (Ma)	Formation temperature range (°C)	Salinity wt.% NaCl equiv.	References
			Pb + Zn (wt.%)	Pb (wt.%)	Zn (wt.%)	Ag (g/t)							
Skarn													
Hetaoping	W. Yunnan, Sanjian Fold System	>2	5–11	0.6–7[3]	0.2–22.4[3]		Cu, Ag	Vein, massive stratiform	Late Cambrian Hetaoping Fm. (marble, slate)	116.1 ± 3.9[1] (Rb–Sr on silicate inclusions in Py and Sp)	98–306[2]	1–11.8[2]	1–2
[a]Luziyuan	W. Yunnan, Sanjian Fold System	1.9		1–2	2.7–4.6		Cu, Ag	Vein, massive stratiform	Late Cambrian Shahechang Fm. (marble)	Late Triassic[4], Mid Permian 266 + 5.4 (U–Pb on zircon)[5]	160–420[6]	3.5–16.1[6]	4–6
Massive sulphide: SEDEX (S) and Volcanogenic massive sulphide (V)													
Dabaoshan (S)	N. Guangdong, Cathaysia Terrane, S. China Fold System	1.5		2.3	5.2	61.9	Au, Ag, Cu	Massive stratiform, lens-shaped	Mid-Late Devonian Dongganglin Fm. (limestone, sandstone)	Devonian[7–8]	280–400[9–10]	1.5–13.2[8]	7–10
Laochang (V)	W. Yunnan, Sanjian Fold System	1.2		2.8	1.1–7.3	12–179	Ag, In, Cd	Massive stratiform, lens-shaped	Early Carboniferous–Permian, Yiliu Fm. (volcanics, carbonaceous rocks)	Early Carboniferous[11–12]	160–350[13]	4.6–17[13]	11–13
[b]Bainiuchang (S)	S.E. Yunnan, Yangtze or South China Craton	1.1		1.6	2.5	92	Cu, Sn	Massive stratiform, vein	Mid Cambrian Tianpeng Fm. (limestone, siltite)	Mid Cambrian [14–15]	52–520[16]	11.5–17.1[16]	14–16
Mississippi-Valley Type													
Huize	E. Yunnan, Yangtze Craton or South China Craton	5	>25				Ag, Ge, Cd	Massive stratifom, lens-shaped	Early Carboniferous, Baizuo Fm. (dolomite, limestone)	225 ± 15.3 (Sm–Nd on calcite)[17]; 176 ± 2.5 (K–Ar on clay minerals)[18]	110–380[19] 165–220[20]	6.2–22.1[19] 6–12[20]	17–20
Niujiaotang	E. Guizhou, Yangtze Craton or South China Craton	0.35			5.9–24.5		Cd	Lens-shaped massive stratiform	Early Cambrian, Qingxudong Fm. (dolostone)	475–499[21] (Pb age model on Sp)	101–142[21]	11–15.9[22]	21–22
Mengxing	W. Yunnan, Sanjian Fold System	0.22	2.6–23.4				Cd, Ag	Massive stratiform, lens-shaped	Mid Silurian, Renhe Fm. (limestone)	Triassic[23–24]	145–161[23]	No data	23–24
Sediment-hosted													
Jingding	W. Yunnan, Sanjian Fold System	>200		1.3	6.1		Cd, Sr	Tabular, vein, massive stratiform	Early Cretaceous, Jingxing Fm. (sandstone, limestone) Tertiary sediments	27–34 (apatite fission track analysis)[25]; 72 ± 4.4 (Re–Os Py)[26]	100–260[27]	1.6–18[27]	25–27

[1]Tao et al. (2010), [2]Chen et al. (2005), [3]Xue et al. (2008), [4]Dong and Chen (2007), [5]Ye et al. (2010), [6]Xia et al. (2005), [7]Yang (1997), [8]Gu et al. (2007), [9]Cai and Liu (1993), [10]Xu et al. (2008), [11]Hou and Li (1998), [12]B.Y. Chen et al. (2000a,b), [13] Li and Tian (1995), [14]Zhou et al. (1998), [15]Zhu et al. (2010), [16]X.M. Chen et al. (2000), [17]Li et al. (2004), [18]Z.L. Zhang et al. (2005), [19]C.Q. Zhang et al. (2005a), [20]Han et al. (2007), [21]Wang (1993), [22]Ye et al. (2000), [23]Li et al. (1985), [24] Deng (1995), [25]Li et al. (2000), [26]Xue et al. (2003), [27]Xue et al. (2007b).

[a] Considered as SEDEX type by Hou et al. (2007).

[b] Considered to be overprinted by hydrothermal activity relating to Yanshanian magmatism (J.S. Liu et al., 2007b; Zhu et al., 2008).

hosted within three main terranes, each separated by major crustal faults: Sanjing Fold Belt System, South China Craton and Cathaysian Terrane (Fig. 1; e.g., Pan et al., 2009; Zaw et al., 2007). A brief characterisation of these deposits is given in Table 1.

Five of the nine deposits are on the western part of South China Terrane within the *Sanjing Fold Belt System* (also called *Sanjing Tethyan Metallogenetic Domain;* STMD). The STMD, with an area of about 160,000 km^2 (Liu et al., 1993), is tectonically situated at the eastern end of the Himalayan–Tethyan tectonic domain, at the junction between the Tethyan Mountain Chain and the Circum-Pacific Mountain Chain (Hou et al., 2007; Mo et al., 1994; Pan et al., 1997). The evolution of STMD consists of the following four successive stages: (i) Late Palaeozoic ocean spreading stage; (ii) Early Mesozoic subduction stage; (iii) Late Mesozoic collisional (orogenic) stage; and (iv) Cenozoic intracontinental orogenic stage (Mo et al., 1994). India–Eurasia collision began before about 55 Ma and the subsequent post-collisional events within the SDMT are considered to be most important stages of its evolution. These relate to uplift of the Himalayas and the Three River Cenozoic orogenic belt, and formed three different structural styles, including: (1) thin-skinned thrust fault and nappe structures developed form outcrop to regional scales, especially in the Lanping–Simao basin; (2) regional high-temperature strike-slip ductile shear zones; and (3) metamorphic core complexes and graben or half-graben basins (Liu et al., 2004, 2006). Most of the mineralization is associated with Cenozoic magmatic and tectonic activity in the region (Hou et al., 2007). As one of the three major volcanic regions in China, it is suggested that STMD is not only one of the key areas for understanding global tectonics, especially Tethyan tectonics, but also one of the World's giant metallogenic belts (Mo et al., 1994).

The southernmost deposit, Laochang, is located within the *Changning Menglian suture zone* and is hosted by Carboniferous alkaline intermediate-mafic volcanics. This deposit that was formed within a VMS system active during the Late Paleozoic. Some authors relate the mineralisation to younger intrusions (Yanshanian–Himalayan; approximately 120–45 Ma; Liu et al., 2010) emplaced underneath the deposit (Pb-isotope models; B.Y. Chen et al., 2000a,b; Xue, 1998). The other three deposits in the Sanjing Fold Belt System, two medium size skarns (Hetaoping and Luziyuan) and a small MVT deposit (Mengxing), are located north of Laochang within the *Baoshan Block*. These are hosted within carbonaceous Early to Mid Paleozoic sedimentary sequences. The two skarns are situated some 150 km apart and mineralisation is considered related to nearby magmatic intrusions of different ages. Whereas Hetaoping relates to Late Yanshanian intrusions (Early Cretaceous), the southern skarn at Luziyuan is considered to be either Late Triassic (Dong and Chen, 2007) or older, i.e., Mid Permian, based on accurate LA-ICPMS U–Pb dating of zircons (Ye et al., 2010). Representing the Early Paleozoic metallogenetic epoch in the Sanjing Fold Belt System, in which mineralization is located in sedimentary basins containing carbonaceous formations, is the Mengxing Mississippi Valley-type (MVT) deposit, located midway between the two skarns. Further north and relating to the Himalayan epoch, the most important mineralizing event in the STMD, is the super-giant (>200 Mt) sandstone-hosted deposit at Jinding, hosted within Cretaceous and Tertiary terrestrial sediments of the *Lanping Basin*. This deposit is the youngest and largest sediment-hosted in the world (Xue et al., 2007a,b) and also one of the highly debated in terms of its genesis.

The *South China Craton* (SCC) (or *Yangtze Craton*), is a major Proterozoic block hosting some of the most important metallogenetic units in China. Its basement is composed by several groups of Proterozoic to Archean rocks, i.e., Kongling, Kangding, Sibao, and Banxi (Li et al., 2002; Qiu et al., 2000; Xu et al., 2007; Zheng et al., 2006). Craton boundaries with the North China and Indochina Blocks are the Qin Lin-Dabie and the Song Ma Suture Zones, respectively (Metcalfe, 2006; Pan et al., 2009). The SCC acted as a coherent tectonic block also during the Phanerozoic, despite the fact that this was a period of complex geological history with metamorphism, granite emplacement, volcanism and rifting along the margins (Zaw et al., 2007). In this study we consider three stratabound deposits in the SCC associated with Early- (Huize and Bainiuchang) and Late Paleozoic (Niujiaotang) orogenic events. The MVT district at Huize is located towards the western margin of the SCC, in the *Sichuan–Yunnan–Guizhou Metallogenetic Region* (Han et al., 2007) and contains some of the largest and high-grade Zn–Pb orebodies in China. The SEDEX deposit at Bainichang is located in the southern-most part of the SCC, in the southeast Yunnan Tin-Polymetallic Metallogenetic Belt. The Bainiuchang deposit was also overprinted by hydrothermal fluids during the Yanshanian orogeny (J.S. Liu et al., 2007; Zhu et al., 2008). The Niujiaotang MVT deposit is located in the central part of the SCC in the *Xiangxi–Qiandong Zn–Pb Metallogenetic Belt*.

Located on the south-eastern edge of the Yangtze Craton, and striking NE, the *Cathaysian Terrane (CT)* (Fig. 1) is made up of several Phanerozoic mobile belts. The northeastern boundary between SCC and CT is the Jiangshao fault. Other boundaries are less well constrained, but most geologists accept that the Jiangnan orogenic belt represents the southwestern boundary. Although the age of the CT basement is still much debated (Shen, 2006; Wang and Zhou, 2006, Xu et al., 2007; Yu et al., 2007, 2009), it is generally suggested that the CT is underlain by Palaeo- to Mesoproterozoic continental crust (Li, 1997; Chen and Jahn, 1998). The CT strata are dominated by metamorphosed or non-metamorphosed Paleozoic to Mesozoic sedimentary sequences and Mesozoic granite (Yu et al., 2007). The *Yuebei Basin* (northern Guangdong Province) is located in the middle of CT. The outer margins of the basin are dominated by pre-Devonian metamorphic rocks, while its cover rocks are Late Palaeozoic, Mesozoic and Cenozoic strata. Devonian strata are abundant in the Yuebei Basin, which overlies the Caledonian unconformity. The basin's edges are mostly controlled by EW- and NNE-trending linear structures; the NNE-trending faults clearly control the distribution of later magmatic intrusions and ore deposits in region, as well as variation in paleogeography (Deng et al., 2005).

The SEDEX deposit at Dabaoshan is located within the Nanling Region (Yuebei Basin) which formed in an intracontinental setting during the Late Paleozoic on the folded Caledonian basement (Gu et al., 2007). The nature of the Zn–Pb mineralisation is debated based on Jurassic ages obtained from Pb-isotope models (e.g., Wang, 2006) or association of the deposit with nearby granites of similar younger ages (e.g., Luo, 1985).

The Yanshanian is the most important metallogenic era in China; over 80% of metalliferous deposits in China were formed in association with large-scale magmatic activity during this period (Chen et al., 2007). The Yanshanian is defined as a tectonic event associated with the westerly oblique subduction of the Izanagi Plate under China's Pacific margin during the Jurassic and Cretaceous (Dong et al., 2007, Hua et al., 2005).

3. Deposit description

3.1. Skarn deposits

The two studied skarn deposits, *Hetaoping* and *Luziyuan*, are small (>2 and 1.9 Mt, respectively) and are located within the Baoshan Block and share several characteristics. They both have protoliths of comparable Late Cambrian age and are positioned distal to the causative intrusions; ~5 km to the N in the case of Hetaoping, and 10 km to the S at Luziyuan (Figs. 2 and 3, respectively). The base metal orebodies are narrow, ranging from 50 to 130 m in width, with lengths varying from 600 to 1050 m, and relatively steep dip. The orefields have strikes of 1.5 and 2 km respectively. At Luziyuan the skarn include also a Fe-orebody consisting of limonite (alteration of

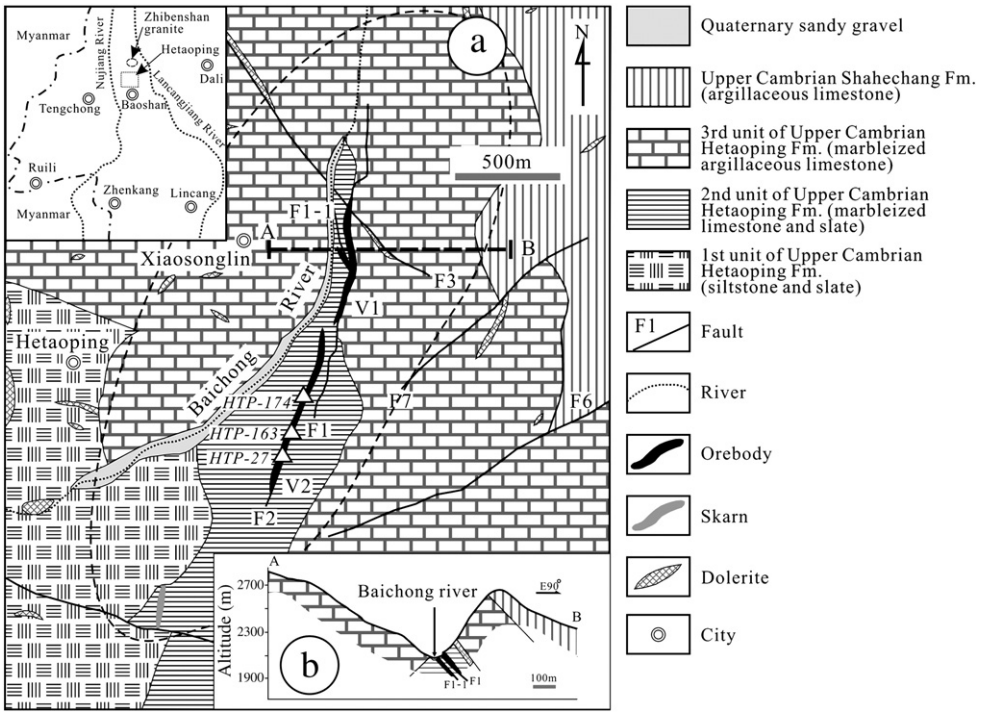

Fig. 2. (a) Geological map of the Hetaoping deposit, and (b) representative cross-section through the deposit. Redrawn after Chen et al. (2005), Zhu et al. (2006) and Tao et al. (2010). The locations of samples used in our study are marked.

magnetite). In both deposits mineralisation is fault-controlled; a N–S-trending fault system is recognised in Hetaoping, whereas the fault-system strikes NE–SW at Luziyuan.

The skarn halo surrounding the ore is narrow, approximately 3 to 10 m, and in both cases, consists of calcic garnet-pyroxene (diopside–hedenbergite) assemblages with retrograde actinolite, tremolite, epidote and chlorite. The Zn–Pb ore is enclosed within the pyroxene skarn close to the marble contact. The actinolite–tremolite skarn is at the boundary between the ore and the pyroxene skarn (Dong and Chen, 2007; Xia et al., 2005; Xue et al., 2006, 2008). Fluid inclusion studies of quartz and calcite in ore samples indicate similar salinity ranges for Hetaoping and Luziyuan, respectively (Table 1; Chen et al., 2005; Xia et al., 2005); no boiling is recognised from these studies. The temperature ranges are also relatively similar (Table 1), reaching

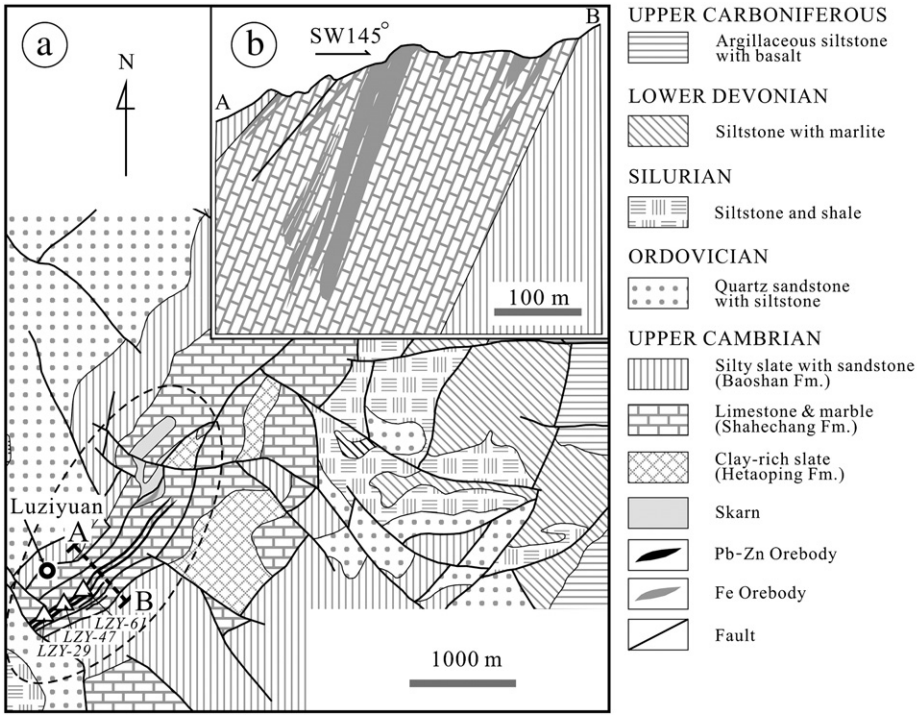

Fig. 3. (a) Geological map of the Luziyuan deposit, and (b) representative cross-section A–B through the deposit. Redrawn after Bureau of Geology and Mining of Yunnan Province (2006). The locations of samples used in our study are marked.

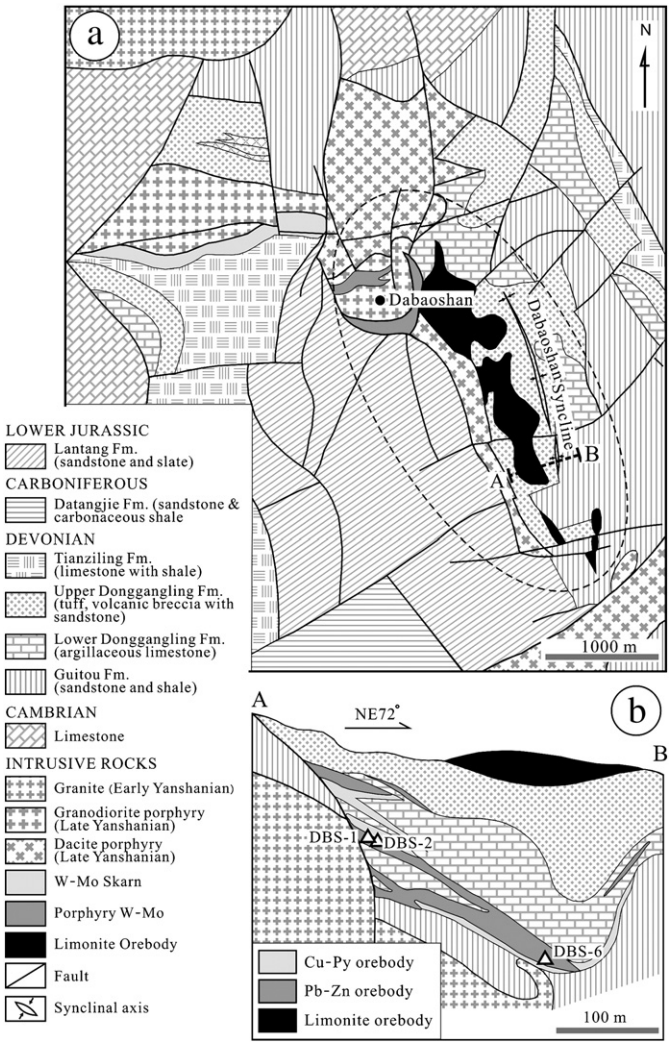

Fig. 4. (a) Geological map of the Dabaoshan deposit, and (b) representative cross-section A–B through the deposit. Redrawn after Wang (2006). The locations of samples used in our study are marked.

upper limits at ~400 °C. Two mineralising stages are suggested for Luziyuan based upon the temperature ranges. S, Pb, O and H isotope studies on both deposits (Xia et al., 2005; Xue et al., 2008) suggest ore deposition as a result of fluid mixing between magmatic-hydrothermal fluids and surficial waters.

3.2. Massive sulphide: SEDEX and VMS

Unlike the skarns the three syngenetic massive sulphide deposits studied here are spread throughout the three major terannes in South China and are all associated with Paleozoic volcano-sedimentary sequences (Fig. 1a; Table 1). The largest (1.5 Mt) is the *Dabaoshan* Zn–Pb SEDEX deposit, located within the Nanling Region of the CT. The massive sulphides are located at the contact between limestone of the Devonian Donggangling Fm. and sandstone–shale sequences of the Guitou Fm. (Fig. 4a,b). The orefield has a 2 km strike with NW–SE orientation and consists of 40 lenses with lengths between 65 and 810 m and thicknesses of 5 to 33 m (Wang, 2006). Copper-pyritic ore is found at the margins of some of the Zn–Pb ores. Two fault systems, trending NW–SE and ENE–WSW, are present of which the former is considered to control ore deposition. Some of the lenses are in direct contact with younger Yanshanian intrusions that have associated W–Mo porphyry and skarn mineralisation (Fig. 4a,b). Small Pb–Zn veins are also found in the northern part of the orefield. Recent age dating (Wang et al., in press) has established a zircon $^{206}Pb/^{238}U$ age of 175.4 ± 1.6 Ma for the Yanshanian granodiorite and a Re–Os age of 163.9 ± 1.3 Ma for associated Mo mineralization.

The mineralising fluids generating the Dabaoshan deposit have a complex, mixed signature based on O, H and S isotopes, i.e., mixing of hydrothermal fluids associated with volcanic activity with seawater or with biogenic S, respectively (e.g., Deng et al., 2005). Fluid inclusions show moderate to high temperatures and salinities (Table 1). He and Ar isotope studies of pyrites from the stratiform lenses and veins indicate their different origins, i.e., concordant with fluids in a SEDEX setting or associated with the Yanshanian granites, respectively (Song et al., 2007). The seafloor SEDEX system has evolved during rapid basin strike-slip extension stage in the Mid-Late Devonian (Deng et al., 2005).

Laochang, situated in the Changning Menglian suture zone, in the southern part of STMD (Fig. 1a,b), is another massive sulphide deposit (1.2 Mt) with a syngenetic origin and has been considered to be of VMS type (Hou et al., 2007). The deposit is hosted within a Lower Carboniferous volcano-sedimentary sequence (Fig. 5a,b), located on the margin of the Laochang caldera at the junction between SN- and NW-trending basement faults. The deposit has a 1.6 km-strike and 200–400 m width, with NW–SE orientation. The orefield consists of some 30 orebodies forming three groups separated by differences in morphology/thickness and host sequence: I: stratiform lenses in

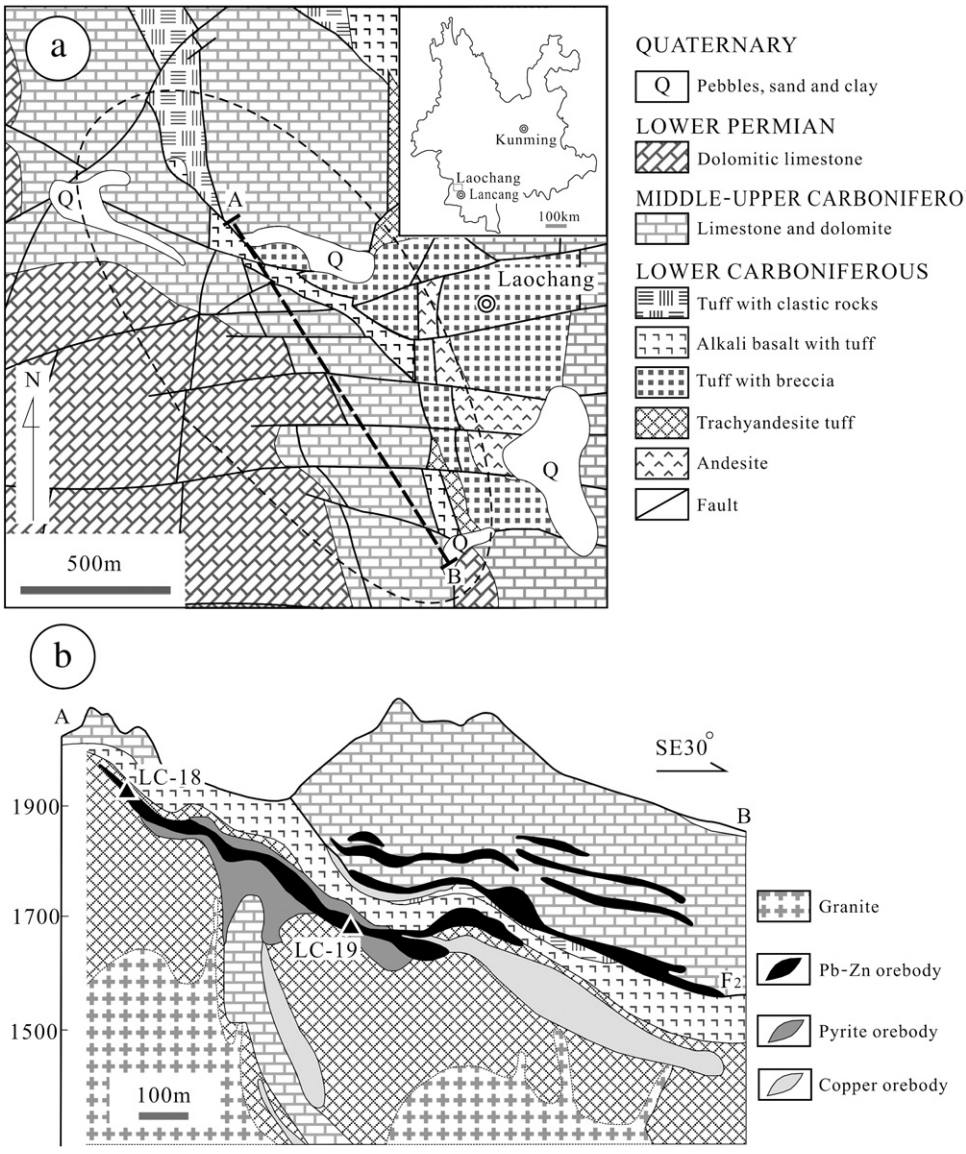

Fig. 5. (a) Geological map of the Laochang deposit, and (b) representative cross-section through the deposit. Redrawn after Li et al. (1996). The locations of samples used in our study are marked.

trachyandesite tuffs belonging to the second cycle; II: stratiform veins in trachyandesite tuffs of the third cycle; III: stratiform lenses in overlaying limestone. Silver is exploited from Ag-rich galena in the orebodies from group II (730–6900 ppm Ag; Li and Tian, 1995). All the samples analysed here come from group I ores (Fig. 5b). Pyrite-galena ores with a strong sulphosalt component are found in the upper part edge of this lens.

As in Dabaoshan, Yanshanian or younger granite intrusions occur adjacent to/underneath the massive orebodies and they have associated Cu–Mo veins that crosscut the volcanic sequence. Re–Os dating of molybdenite from such veins gave an age of 43.7 ± 0.78 Ma (Li et al., 2010) which is concordant with the Rb–Sr age obtained from sphalerite–pyrite grains in the massive ore (45 ± 3.6 Ma; Long, 2009) but much younger than U–Pb ages obtained from zircon in the nearby granite (126.7 ± 3.5 Ma to 529.3 ± 13 Ma; Li et al., 2010). Fluid inclusions show moderate to high temperatures and salinities (Table 1). Lead, S, C, O and H isotopes show a mixed magmatic and seawater signature for the VMS ore where the Pb may have been leached from different strata in the basin. A second, different magmatic signature is also recognised and this is associated with the granite emplacement (e.g., Long, 2009).

The third syngenetic massive sulphide deposit is *Bainiuchang*, a small (1.1 Mt) SEDEX deposit located in the Yunnan Tin-Polymetallic Metallogenetic Belt of the SCC (Fig. 1a), and hosted by Mid-Cambrian sediments. The orebodies form stratiform lenses hosted within dolomite, limestone and sandstone of the Tianpeng Fm. (Fig. 6). The 5 km-long, NW–SE-striking orefield is 2 km in width. The deposit consists of 40 lenses grouped into 5 ore blocks. The lenses have length between 50 and 500 m in thickness between 0.7 and 7 m. Our sampling was undertaken in the Duimenshan orebody, one of the few areas accessible in the mine, which is currently in its final stages of operation. Besides a large Ag reserve (>7000 t; Xie et al., 2009) the ores have also a prominent Sn signature with reserves of 86,000 t Sn (J.S. Liu et al., 2007) and a broad range of other elements noted (In, Cd, Ge, Ga; Xie et al., 2009). The orefield is ~7 km SW of the large (~120 km^2) Bozhushan Yanshanian granite and some smaller granite bodies were intersected in exploration drillcores (J.S. Liu et al., 2007). As in the other two areas with syngenetic massive sulphides, here there is a debate about the role of granite-related fluids in formation of the base metal ores. Stable isotope studies show that the sulphides clearly relate to two distinct events, one during the Mid Cambrian (SEDEX system) and a second during the Yanshanian orogeny (Xie et al., 2009). Fluid inclusion studies show

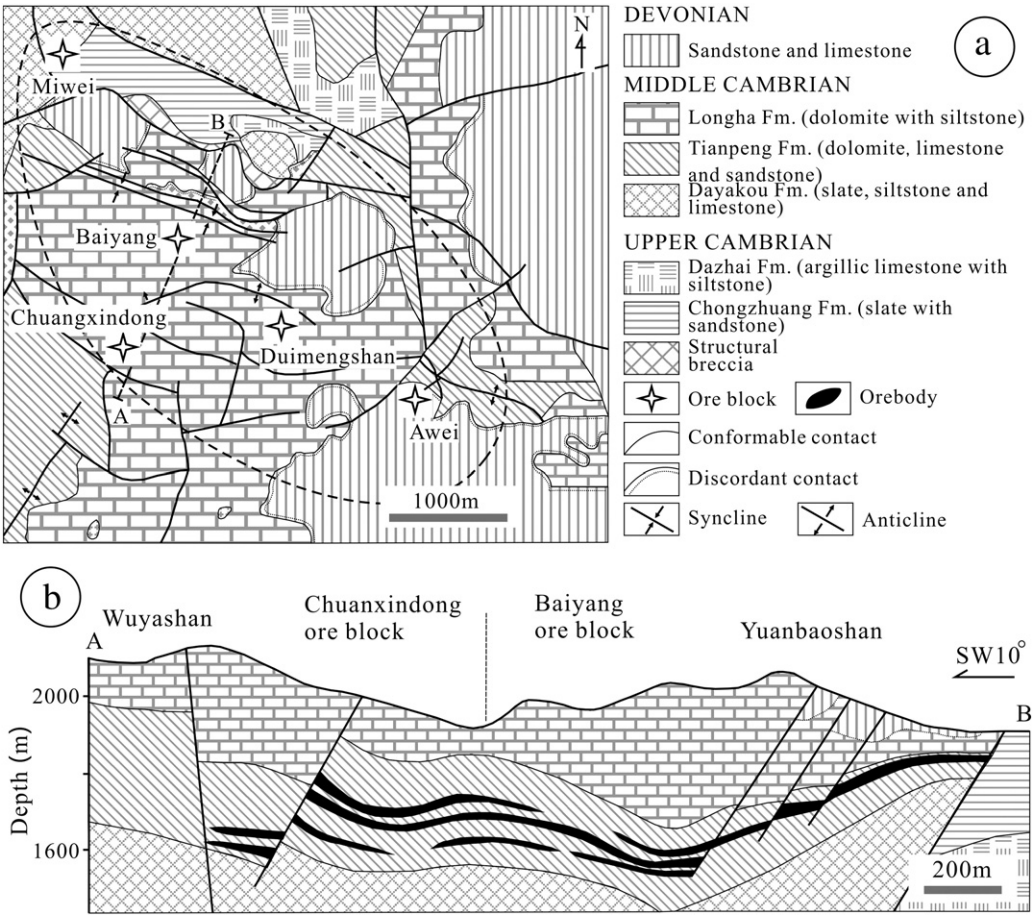

Fig. 6. (a) Geological map of the Bainiuchang deposit, and (b) representative cross-section. Redrawn after Xie et al. (2009).

moderate to high temperature and relatively high salinities (Table 1; X.M. Chen et al., 2000).

3.3. Mississippi-Valley-type deposits

Another group of sulphide deposits studied here, generally smaller in size than the main syngenetic deposits discussed above, are epigenetic in origin and have been considered to be of MVT type. The MVT deposits are all located in the same geographic province, Yunnan, but belong to two main tectonic domains, SCC and STMD. The MVT ores are hosted within carbonaceous sequences from the Paleozoic basins which are widespread in the region. Their age is, however, considered younger, possibly spreading into the Mesozoic.

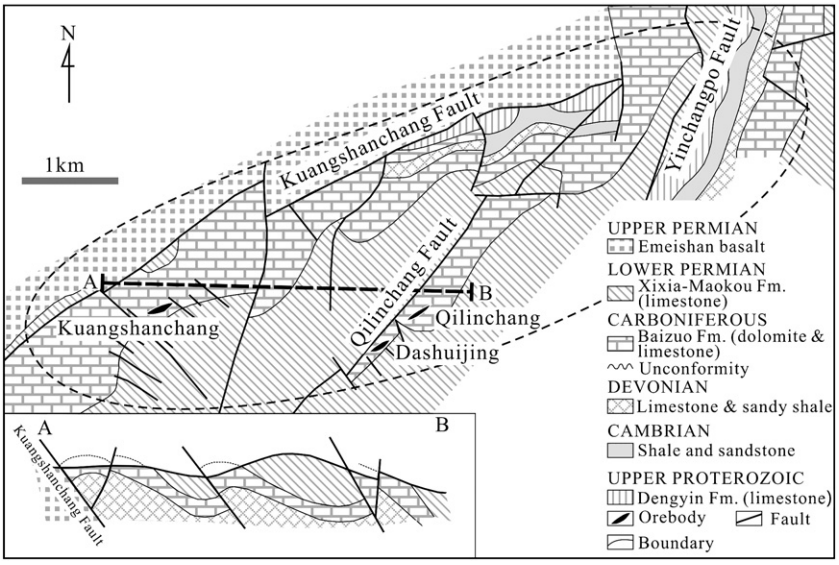

Fig. 7. Geological map of the Huize deposit, redrawn after Han et al. (2007).

The largest (5 Mt) is *Huize*, a Zn–Pb–(Ag) MVT district located in the south-central part of the Sichuan–Yunnan–Guizhou Metallogenetic Region (Fig. 1a) on the south-western margin of the SCC and on the eastern side of the Xiaojiang deep fault zone (Kang, 1982). The Huize district is located within the Kuangshanchang fault system (ESE–WNW trending), which is part of the regional Xiaojiang fault zone. The ores are hosted within dolomite and limestone of the Carboniferous Baizou Fm. The orefield has an ESE–WNW strike with a length of ~10 km and a width of ~1.5 km (Fig. 7). The district contains >50 orebodies constituting three deposits (oreblocks), separated by faults with NNE–SSW orientation: Kuangshanchang to the SW (42 orebodies), Qilinchang (including Dashuijing; 8 orebodies) in the central southern part and Yinchangpo to the NE (Han et al., 2007). The most important are orebody 1 in the Kuangshanchang deposit and orebodies X, VIII and VI in the Qilinchang deposit; our samples were collected from the latter orebody. Orebody VI is the largest, with >800 m strike, thicknesses between 0.7 and 40 m and >1200 m extension along dip. Orebodies from the Qilinchang deposit are located within an interstratified fault zone between the middle and upper levels of the Baizou Fm. Orebody composition varies

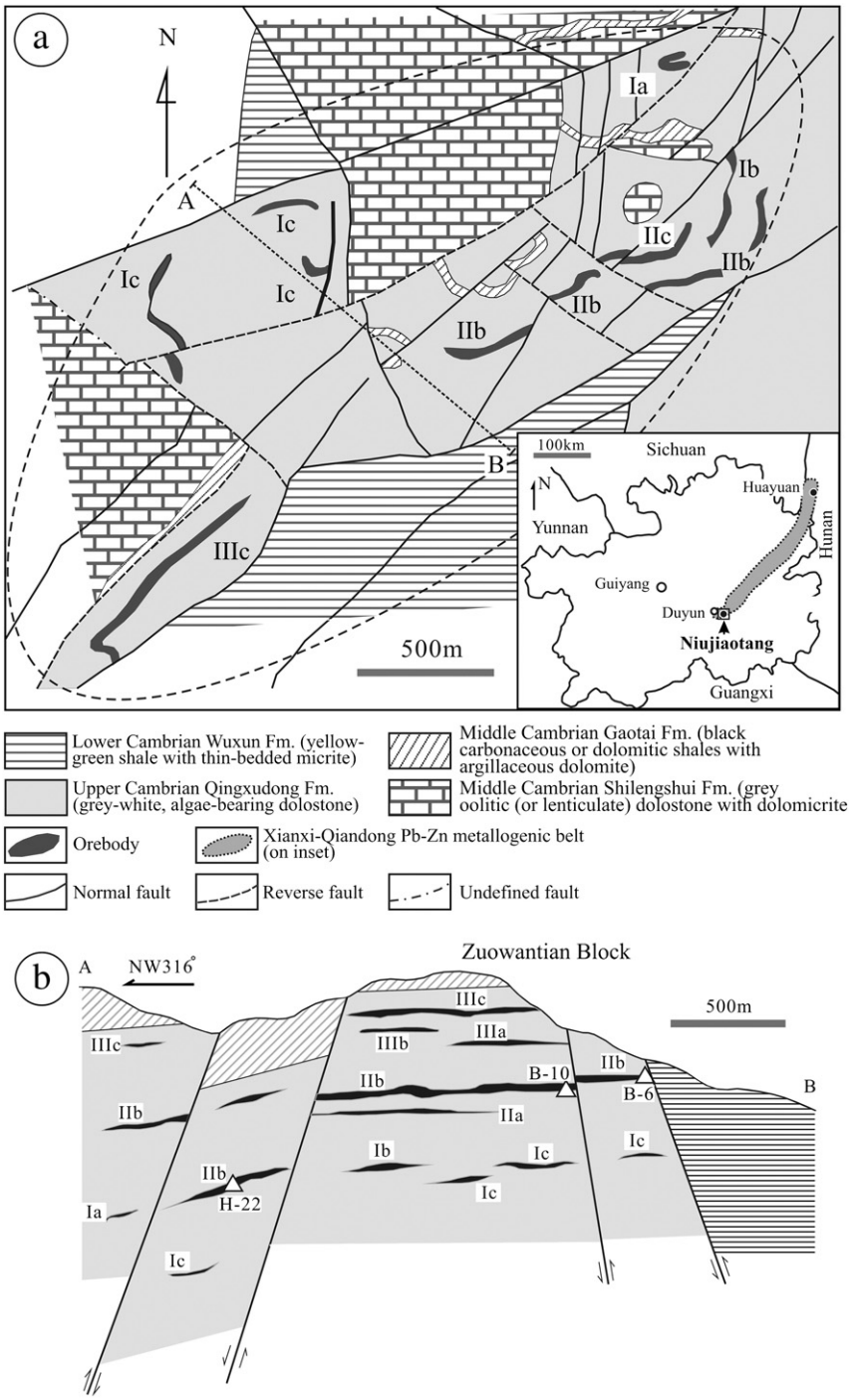

Fig. 8. (a) Geological map of the Niujiaotang deposit, and (b) representative cross-section through the deposit. Redrawn after Chen et al. (1992). The locations of samples used in our study are marked.

gradationally from the upper (oxide) to deeper (sulphide) parts. Ore grades are very high (>25 wt.% Zn + Pb) and are enriched in Ag, as well as a range of other elements such as Ge, In, Ga, Cd and Tl (Han et al., 2007).

Whereas the stratabound character of the deposits was recognised and accepted by most authors, the origin of the metal sources has been a long-lasting debate (see Han et al., 2007). Early classifications of Huize, such as 'sedimentary-reworked' (e.g., Tu, 1988) or 'Emeishan basalt magmatic hydrothermal mobilisation and enrichment during Indonisian–Yanshanian tectonic localisation' (e.g., Huang et al., 2003) suggested that the metal sources have a syngenetic component but the mineralisation is the result of multi-stage hydrothermal events associated with different orogenies. More recent studies (e.g., Zhou et al., 2001) assigned the Qilinchang deposit to a MVT-style genesis. The latest fluid inclusion and isotope studies indicate a low temperature range, <220 °C, relatively high salinities (Table 1) and suggest that the fluids were mainly derived from the Kunyang Group basement rocks and evaporite-bearing rocks in the cover strata (Han et al., 2007). Such studies conclude that the sulphides are not of carbonate-replacement type but rather represent deformed, carbonate-hosted MVT-type ores.

The second deposit discussed here is *Niujiaotang*, a small (0.35 Mt) MVT deposit which is located at the southern margin of the Xiangxi–Qiandong Zn–Pb Metallogenetic Belt, in SCC (Figs. 1a and 8). The orefield lies parallel to the Zaolou fault system (NE–SW orientation) which is related to the Mandong NE-trending regional fault. The Zaolou fault is considered to have been active during the Mid-Late

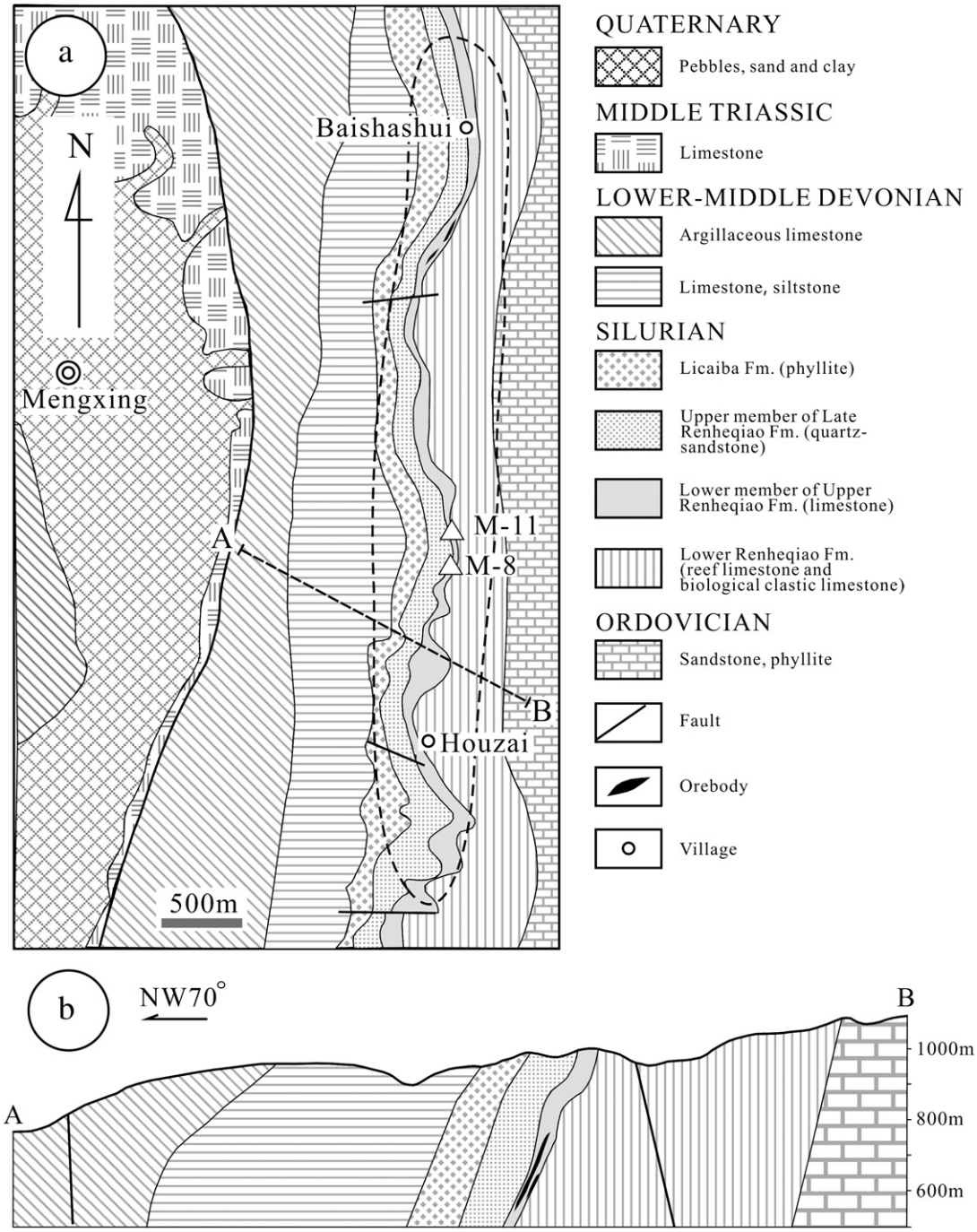

Fig. 9. (a) Geological map of the Mengxing deposit, and (b) representative cross-section A–B. Redrawn after Li et al. (2005). The locations of samples used in our study are marked.

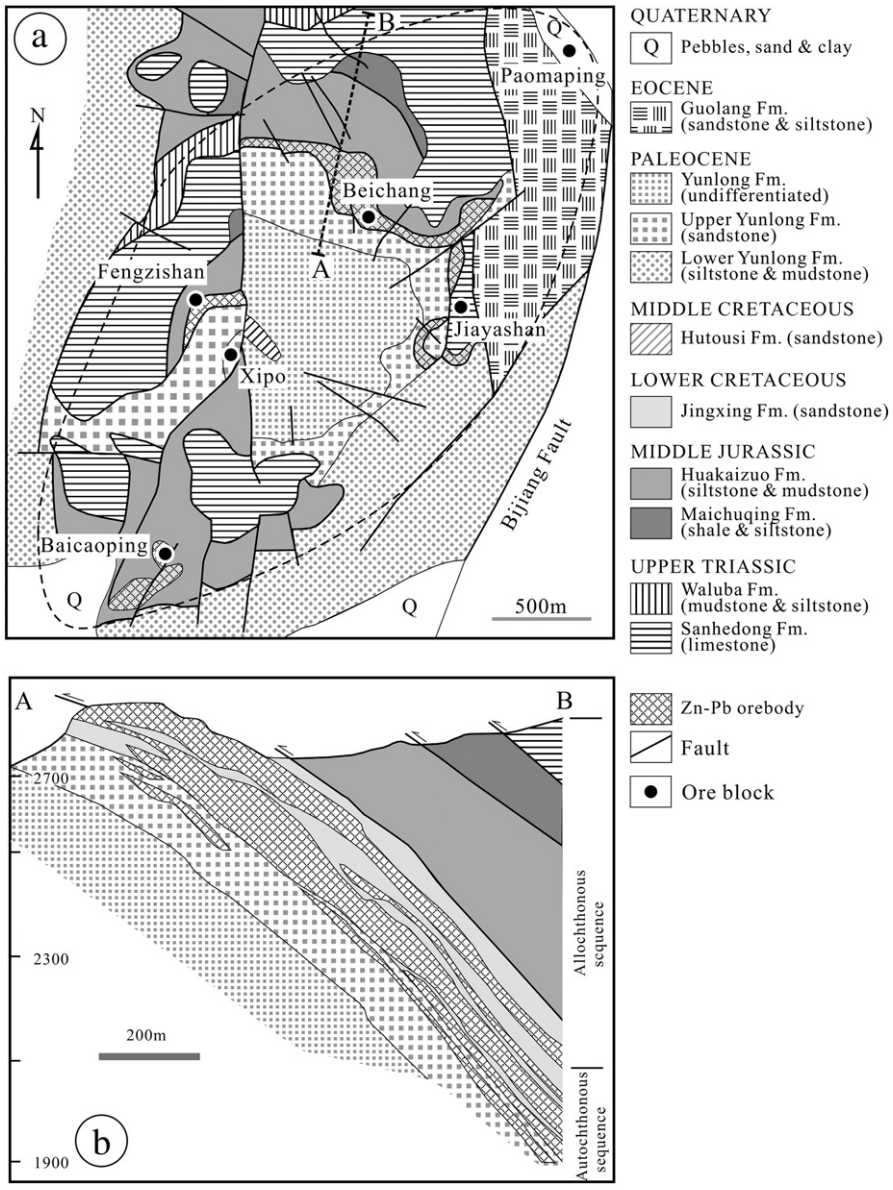

Fig. 10. (a) Geological map of the Jinding deposit, and (b) representative cross-section A–B. Redrawn after Xue et al. (2007b).

Caledonian orogeny. Niujiaotang is one of the largest of 10 deposits of similar type in this belt and has been recently reviewed by Ye et al. (in press). The ~3 km-long orefield strikes NE–SW and is 1.5 km in width (Fig. 8). The ores form stratiform, horizontal lenses within the Cambrian algae-bearing dolomite of the Qingxudong Fm. There are some 10 orebodies grouped into four blocks separated from one another by a series of faults perpendicular to the deposit strike. Orebody IIb from the central, Zuowantian block (sampled for this study), is the largest (500 m wide, 850 m long, with thicknesses from 0.3 to 20 m) and has a gentle dip towards SW. The deposit is Cd-rich (mean 1.38 wt.%; Ye and Liu, 1999).

Fluid inclusion studies indicate involvement of low temperature (<150 °C) and relatively high salinity (11 to 15.9 wt.% NaCl equiv., Table 1; Ye et al., 2000) fluids. Sulphur and Pb isotope studies (Ye et al., 2005) indicate that the sulphur source is in the oil-field brines within the Qingxudong Fm., whereas the metals (Zn and Pb) are mainly derived from the underlying strata (Early-Cambrian Wuxun Fm.). These interpretations, as well as the Ordovician age (Pb-isotope model on sphalerite; Table 1; Wang, 1993) suggested for the mineralisation, are all concordant with an epigenetic origin for the massive sulphides.

Mengxing, the smallest (0.2 Mt) MVT deposit we have studied, is located within the Baoshan Block from the STMD domain (Fig. 1a,b). The ores are hosted within limestone of Mid-Silurian Renheqiao Fm. and the orefield, ~3 km in length and ~500 m in width, has a NE–SW to N–S strike is situated along a monocline structure (Fig. 9). There are 32 individual orebodies with lengths varying from 15 to 1200 m, widths between 60 and 600 m, thicknesses between 0.25 and 10 m; all with high-angle dips towards SW.

The mineralisation is considered to be of MVT-style based on the stratiform and stratabound character of the ores and general geology of the basin (Deng, 1995). Fluid inclusion studies indicate low-temperature fluids with moderate salinities (Table 1; Li et al., 2005).

3.4. Sandstone-hosted deposits: Jinding

The last deposit under discussion, *Jinding*, is one of the largest and youngest sediment-hosted Zn–Pb deposits in the world (>200 Mt). Jinding is located in the northern part of the Lanping Basin from STMD (Fig. 1a,b). The Lanping basin, filled with Cretaceous and Tertiary terrestrial sediments, has developed as an intracontinental structure

Table 2
Overview of samples investigated in this study, mineral assemblages and key ore textures.

Deposit, orebody, sample no.	Location	Ore assemblage	Form and location of ore	Ore textures
Hetaoping, orebody V/1				
HTP-27	Mine 88, Level 1950 m	Sp, Gn, Py	Massive Zn ore in actinolite skarn	Replacement of Sp by Gn; late Py inclusions.
HTP-163	Mine 88, Level 1950 m	Sp, Gn, Py	Massive Zn ore in marble	Herring-bone texture Gn in Sp, 'flower'-like intergrowths of Sp and carbonate, late replacement of Sp by Py.
HTP-174	Mine 55, Level 2150 m	Sp, Cp, Py, Gn, Bn	Massive Zn-Cu ore in marble	Marginal replacement by Py, Cp and Bn; erratic Cp exsolutions in Sp.
Luziyuan, orebody II				
LZY-47	Level 1360 m	Sp, Gn, Cp, Py, Apy, Mt, minor Cos	Massive/patchy Zn ore in pyroxene skarn	Gn–Cos intergrowths in Cp elongated domains; zoned and brecciated, inclusions of Py and Apy
LZY-29	Level 1360 m	Sp, Cp, Gn, Py, Mrs	Massive/patchy Zn–Pb ore in marble	Gn and Cp at the margin of Sp grains; Mrs formed by replacement of Po
LZY-61	Level 1360 m	Sp, Py, Mt, (Gn)	Massive Zn ore in actinolite skarn	Inclusions of Mt, Py, Gn and actinolite
Dabaoshan, orebody 1, first layer of massive Zn ore				
DBS-1	Level 650 m	Sp, Gn, Py, (Cp)	Massive Zn–Pb ore and quartz-carbonate rock	Gn as inclusions in Py; late brecciation with replacement of ore by gangue minerals; fractures crosscutting large Py and Sp; small Py grains along discrete veinlets
DBS-2	Level 650 m	Sp, Gn, Py, Mt, (Cp)	Massive Zn–Pb ore and quartz-carbonate rock	Highly porous margins of Sp with Mt replacement; erratic Cp exsolutions
DBS-6	Level 500 m	Sp, Gn, Py, (Cp, Apy)	Massive Zn–Pb ore in carbonate rock;	Exsolution of Cp in Sp; Py as idiomorphic grains and porous aggregates; ore is fractures and replaced by gangue minerals
Laochang, orebody I				
LC09-109	Level 1625 m	Sp, Py, Mrs, Gn, (Cp)	Massive and disseminated Zn ore in carbonate rock;	Complete replacement of Po by Mrs; coarse Py is brecciated and replaced by Gn, Cp and Mrs, especially along the grain boundaries with Sp; rare exsolution of Cp in Sp
LC-18	Level 1910 m	Sp, Gn	Massive Zn–Pb ore in andesite tuff	Discrete brecciation
LC-19	Level 1700 m	Sp, Py, Mrs, Gn, Cp, Po	Massive, coarse Zn–pyritic ore in andesite tuff;	Po inclusions in Py; fine-grained, botryoidal Mrs with Py nucleating along veinlets and within cores; strong brecciation of all ore minerals with replacement of gangue minerals; marginal corrosion of Py with replacement of Sp, Gn and Cp
Bainiuchang, Duimenshan orebody				
BNC-3	Level 1480 m	Sp, Gn, Py, (Cp)	Massive Zn–Pb ore in limestone	Dense, cleavage oriented exsolutions of Cp in Sp; Py replacement along cleavages
BNC-10	Level 1480 m	Sp, Gn, Po, Mrs, Cp, Py	Massive Zn–Pb ore in limestone	Partial replacement of Po by Mrs; Dense Cp exsolutions on Sp; Mrs with Py cores; Strong brecciation with replacement of sulphides by gangue minerals
Huize, orebody VI				
HZF-1086	Level 1764 m-section 12	Sp, Gn, (Py)	Massive Zn–Pb ore in dolomite	Sp has domains of high porosity outlined by fractures filled with fine-grained Py and Gn; the same on discrete fractures throughout Sp
HZF-1062	Level 1764 m-Section 8	Sp, Gn, Py, (Hm)	Massive Zn–Pb–pyritic ore in dolomite	Small-grained, idiomorphic Py, some skeletal-shaped overprinting the Gn–Sp boundaries
HZF-1065	Level 1764 m-Section 8	Sp, Gn, (Py)	Massive Zn–Pb ore in dolomite;	Dusty inclusions of Py in Sp; Py also along fractures in Sp
Niujiaotang, orebody II-b				
B-6	Level 730 m	Sp, Py, (Grk, Gn)	Patchy Zn-pyritic ore from the oxidised zone nearby major fault in dolomite	Masses of fine-grained Py; discrete fractures with Grk ± Gn
B-10	Level 730 m	Sp, Py, (Gn, Grk)	Massive Zn–pyritic ore from the oxidised zone nearby major fault in dolomite	Fractures with secondary, Cd-rich Sp and Grk ± Gn
H-22	Level 650 m	Sp, Py, (Gn)	Nodular Zn–pyritic ore in dolomite	Nodule zonation: dark cores to light-brown margins; dusty inclusions of Gn in Sp
Mengxing, orebody III				
M-8	Level 920 m	Sp, Py, Gn	Banded Zn–Pb–pyritic ore in limestone	Sp as idiomorph inclusions in coarse Py enclosed within masses of Gn; Fluidised textures in massive Sp underlined by fringes of fine-grained Py and gangue minerals (Qz and carbonate) also with interstitial replacement by carbonate
M-11	Level 920 m	Sp, Py, Gn	Massive Zn ore grading into to interstitial Zn–pyritic ore in limestone	Nodular Py–Sp bodies (consisting of fine-grained Py and rounded, porous Sp) and skeletal Py in Gn; Py with collomorph texture growing into coarse, idiomorph grains; Sp brecciated with fluidised domains; brecciated Sp cemented by Gn and interstitial fine-grained Py and carbonate

(continued on next page)

Table 2 (*continued*)

Deposit, orebody, sample no.	Location	Ore assemblage	Form and location of ore	Ore textures
Jinding				
JD148	Beichang orebody Level 2630 m	Py, Mrs, (Sp, Gn)	Massive pyritic-base metal ore in carbonate rock	Coarse Py/Mrs aggregates; overgrowths of fine Py on coarse cores; brecciation followed by precipitation of interstitial Sp; Sp also as inclusions in Py/Mrs
JD155-26	Paomaping orebody Level 2380 m	Sp, Gn, (Py, Mrs)	Disseminated Zn ore in 'arkose' cemented by carbonate	Coarse grading into fine-grained Sp with interstitial Gn and carbonate; Sp replacement after lamellar mineral; rounded, 'strawberry'-like formations in Sp outlined by carbonate; small, collomorph, skeletal and framboidal Py
Jinding				
JD91-2	Jiayashan orebody Level 2695 m	Sp, Gn, (Py)	Disseminated Zn ore in carbonate rock	Fine-grained, porous aggregates of Sp grading into sparse disseminations; interstitial bodies of Gn; larger Gn with Sp inclusions along lineaments spanning into the carbonate matrix; Py along fractures
JD150	Jiayashan orebody Level 2585 m	Sp, Gn, (Py)	Zn–Pb ore interstitial to sandstone	Fine-grained aggregates of Sp with high porosity; in some grains this is marginal to a more compact aggregate core; usually Gn on the margins of such Sp aggregates; locally tendency towards idiomorphic edges; abundant barite inclusions with dusty Gn in Sp

Apy—arsenopyrite; Cp—chalcopyrite; Gn—galena; Grk—greenockite; Hm—hematite; Mrs—marcasite; Mt—magnetite; Po—pyrrhotite; Py—pyrite; Sp—sphalerite.

within the Changdu–Lanping–Simao micro-plate situated between the Yangtze Plate to the E and the Tibet–Yunnan Plate to the W; these domains are separated from one another by the Ailaoshan Red River and Chongshan Cenozoic shear zones (Liu et al., 2011). The deep crustal Lanping–Simao fault is in the centre of the basin (e.g., Jin et al., 2003). Tectonic evolution of the basin includes the following five tectono-magmatic stages (Liu et al., 2004, 2006, 2010):

1st stage — Regional shortening related to the Indian–Eurasian collision; formation of wide, thin-skinned thrust faults and nappe structures at different scales. Although allochthonous rocks are predominantly Triassic, they can locally be either older (Devonian or Ordovician) or younger (Jurassic or Cretaceous), whereas the autochthonous rocks are Jurassic to Paleocene;

2nd stage — Post-collisional high-K alkaline magmatic activity at 43–30 Ma along the eastern boundary of the Indochina Block (Liang et al., 2007); formation of a large-scale Cu–Mo–Au and Pb–Zn ore province (e.g., Dali) related to post-collisional extension on the eastern side of the Ailaoshan Red River Shear Zone;

3rd stage — Regional strike-slip shearing, forming upper crustal brittle strike-slip faults in the basin and middle to lower crustal ductile shear zones on both sides of the basin at 35 to 21 Ma (Zhang et al., 2006);

4th stage — A regional extensional event in a fan-shaped area between the Red River and Sagaing Faults in S.E. Asia during the Early Miocene (J.L. Liu et al., 2007), forming metamorphic core complexes, grabens, and half-grabens;

5th stage — Right-lateral shearing associated with a shallow crustal event at 8 Ma to present-day, mainly along the Red River Fault.

The ore is mostly hosted within and at the boundary between sandstone and limestone sequences of different ages, i.e., Paleocene Yunlong Fm. in the footwall and Early-Cretaceous Jingxing Fm. in the hanging wall (Fig. 10). There are more than 100 orebodies distributed within six clusters around the Jinding Dome. Sampling was undertaken from three of the north-eastern clusters: Jiayashan, Beichang and Paomaping; the former is the largest in the orefield (1450 m length, 1260 m deep and 10–70 m thick — making up about 40% of the total ore mass at Jinding; Zhao, 2007). Most of the mineralisation in this part of the deposit consists of secondary Zn-oxides (supergene enrichment in the oxidation zone) whereas Beichang and Paomaping preserve more of the primary sulphides. Whereas sandstone-hosted ores and their supergene counterparts contribute to production at Jiayashan and Beichang, limestone-hosted ores are the mainstay of mining in Paomaping. Fluid inclusion studies of sphalerite and associated gangue minerals give temperatures up to 300 °C, clustering around 110 to 150 °C, with widely varying salinities (Table 1; Xue et al., 2007a). Sulphur isotope ratios vary widely and suggest that thermo-chemical bacteria sulphate reduction assisted sulphide deposition (Xue et al., 2007a).

The deposit genesis is strongly debated since the 1980s with authors favouring either a syngenetic or epigenetic origin (see Xue et al., 2007a for discussion). Deposit characteristics share features of both types of mineralisation but many recent isotope, fluid inclusion and fluid-flow modelling studies have shown that Jinding is rather unique. In particular, the involvement of CO_2-rich mantle sourced fluids (fluid inclusions, Pb and noble isotopes studies) in an intracontinental terrestrial basin with an active tectonics with respect to plate collision are emphasised (Xue et al., 2007a,b). Dynamic modelling of fluid flow in the basin shows that the overpressures indicated by the CO_2-rich inclusions ($513–1364\times10^5$ Pa; Xue et al., 2007b) cannot be produced by either sediment compaction or thrusting. They can be explained instead by pressure building in the basin during injection of mantle fluids. Mixing of such high-T, lower salinity mantle fluids with lower-T, higher salinity basinal fluids may be the key process to explain the large-scale mineralisation occurring during formation of the Jinding Dome (structural-lithological trap).

4. Sample description

Sphalerite is either the main component or is present in some abundance in all the studied deposits. The suite of samples is representative of the different deposit types even though is not comprehensive at the scale of each deposit but rather limited to those parts of one or the other orebody within the deposit which were accessible for sampling (Table 2). Some of the characteristics of individual deposits, and in particular their geochemical signatures, are presented below.

Sphalerite in samples from the *Luziyuan* and *Hetaoping* skarn deposits is relatively Fe-rich (from 3 to 10 wt.%; see below). Variation in the Fe content along strike is observed in both cases; in Hetaoping the Fe content also increases with depth. In Hetaoping sphalerite shows primary textures such as herring-bone intergrowths with galena (Fig. 11a), suggesting simultaneous deposition in equilibrium, as well as overprinting features such as corrosion boundaries marked by replacement of sphalerite by carbonate and pyrite; some of the latter minerals also form discrete grains or aggregates within areas of high porosity in sphalerite (Fig. 11b,c). Replacement along cleavages by actinolite and galena is also noted in sphalerite (Fig. 12a). In Luziyuan sphalerite contains inclusions of magnetite (Fig. 11d) and is associated with early pyrrhotite. The latter is replaced by pyrite

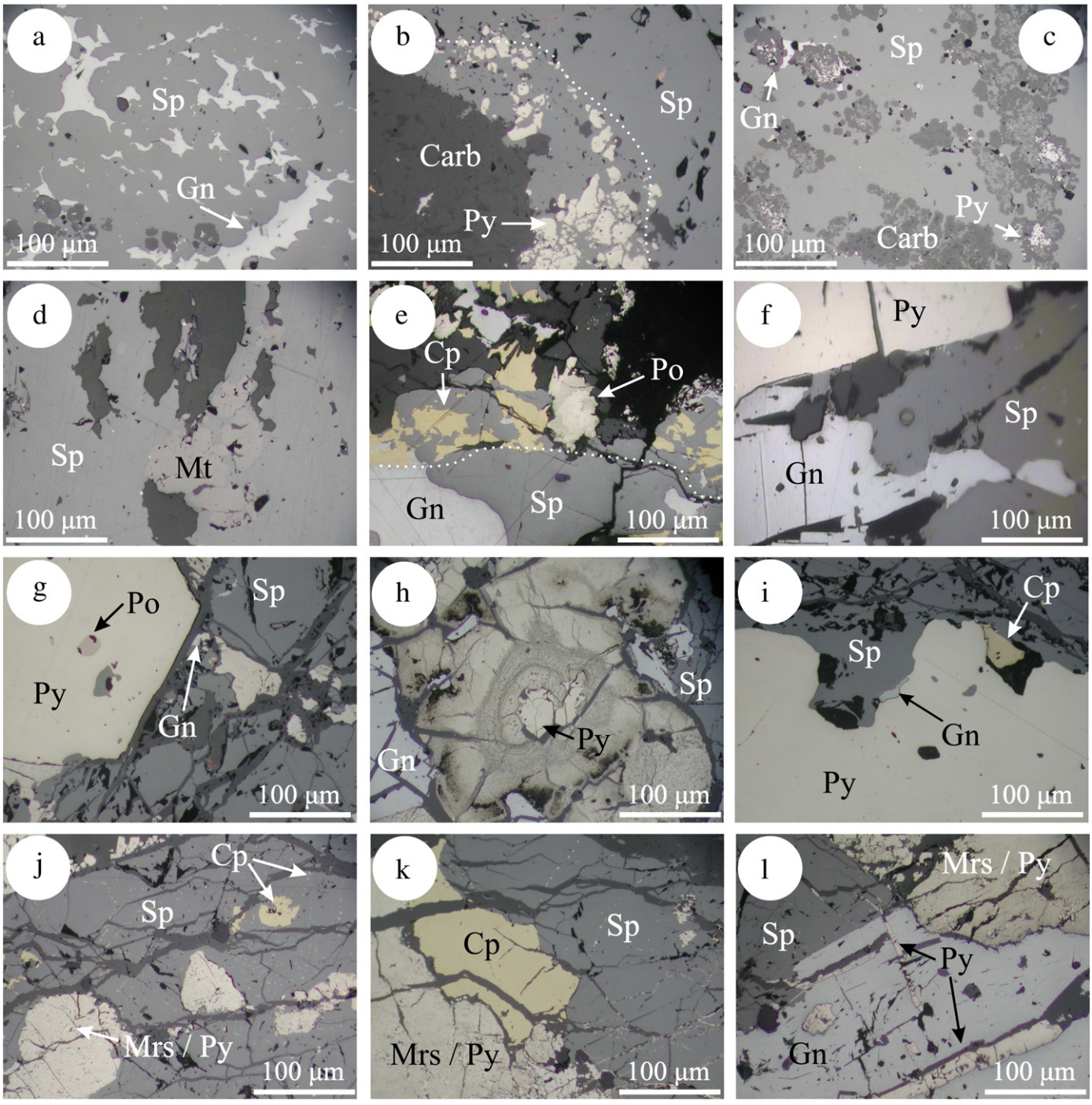

Fig. 11. Photomicrographs in reflected light illustrating textures and structures in the Pb–Zn ores from the Hetaoping, Luziyuan, Dabaoshan, Laochang and Bainiuchang deposits. (a) Herring-bone texture of sphalerite (Sp) intergrowths with galena (Gn) (Hetaoping, HTP-163). (b) Corrosion boundaries marked by replacement of sphalerite by carbonate (Carb) and pyrite (Py) (Hetaoping, HTP-174). (c) Carbonate and pyrite form discrete grains or aggregates within areas of high porosity in sphalerite (Hetaoping, HTP-163). (d) Microinclusion of magnetite (Mt) in sphalerite associated with early pyrrhotite (Luziyuan, LZY-61). Pyrrhotite not seen in photograph. (e) Sphalerite replaced by galena (Gn) and chalcopyrite (Cp) (Luziyuan, LZY-29). Marcasite (Mrs) after pyrrhotite (Po). (f) Corrosion texture suggestive of galena dissolution and replacement by sphalerite (Dabaoshan, DBS-2). (g) Pyrrhotite (Po) inclusions in pyrite (Py); minor galena replaced by sphalerite (Dabaoshan, DBS-1). (h) Recrystallised colloidal pyrite and xenomorphic pyrite nucleating in the cores (Laochang, LC-19). (i) Pyrite replaced by sphalerite associated remobilisation of minor galena and chalcopyrite along the replacement boundaries (Laochang, LC-19); (j) Relict pyrite (altering to marcasite) partially replaced by sphalerite (Laochang, LC-19), which is fractured. (k) Micron-scale inclusions of chalcopyrite in sphalerite (Bainiuchang, BNC-10); (l) Replacement of galena by sphalerite and brecciated marcasite-pyrite-(pyrrhotite) (Mrs/Py) and crosscut by late pyrite veinlets (Bainiuchang, BNC-10).

during episodes of brecciation, also accompanied by formation of chalcopyrite and Bi-minerals (cosalite, native bismuth; Figs. 11e and 12b). There is some supergene replacement of pyrrhotite by marcasite. Grain-scale mobilisation of the more ductile galena and sulphosalts is observed within fractures in euhedral arsenopyrite enclosed in sphalerite (Fig. 12c, d). The high-Fe content in sphalerite indicating reduced fS_2 fluids is compatible with the presence of hedenbergite, pyrrhotite and magnetite, suggesting its formation at the end of the prograde skarn stage or possibly during the retrograde sulphide stage, in a distal position from the fluid source (adjacent to the marble contact; c.f. Ciobanu and Cook, 2004). The textures above clearly show that sphalerite has been affected by the retrograde fluids,

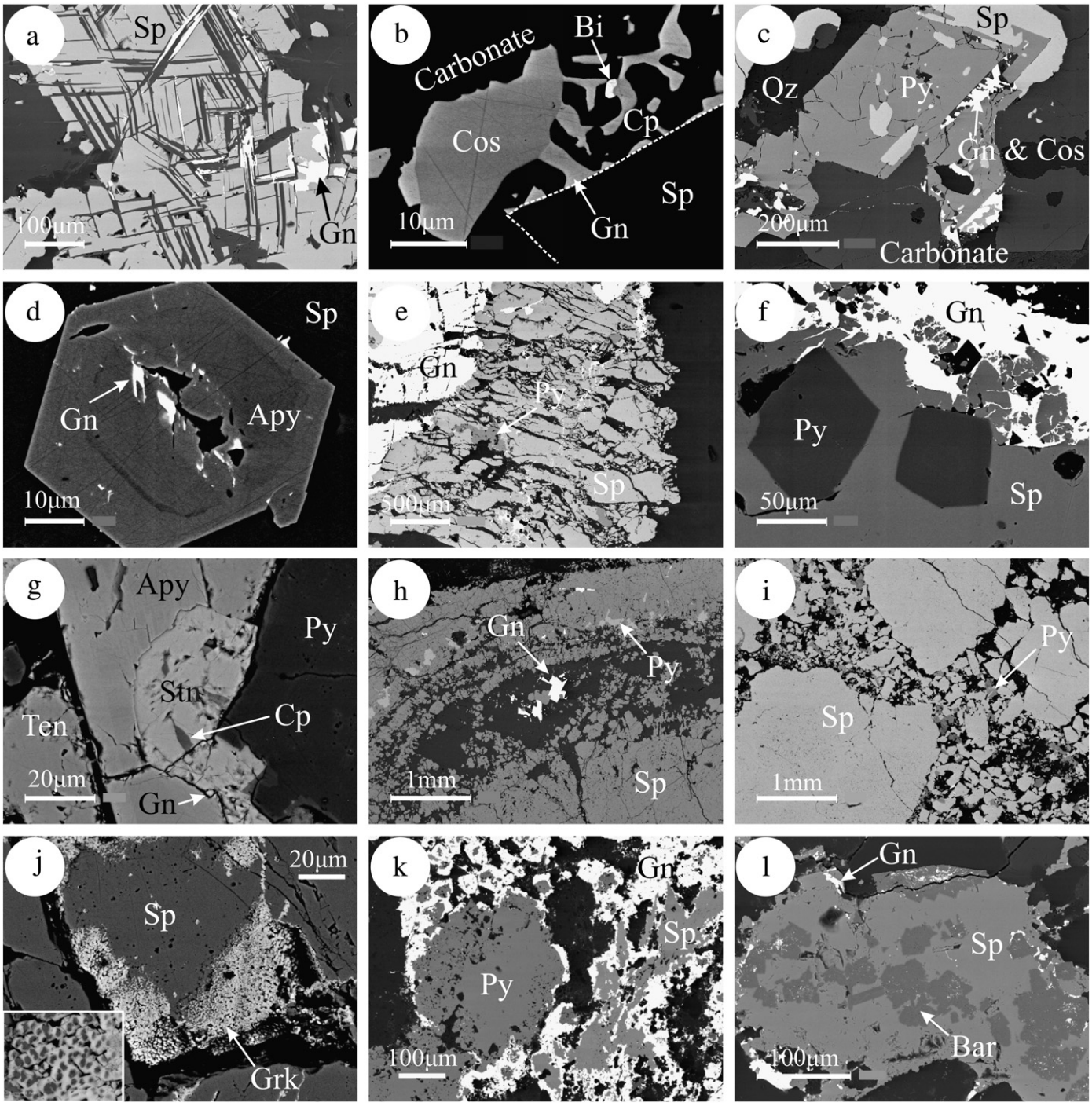

Fig. 12. Back-scatter electron images showing aspects of the Pb–Zn ores from Hetaoping, Luziyuan, Dabaoshan, Laochang, Niujiaotang and Jinding. (a) Replacement along cleavages by actinolite and galena (Gn) in sphalerite (Sp) (Hetaoping, HTP-27). (b) Replacement of sphalerite (Sp) by chalcopyrite (Cp), galena (Gn) and Bi-minerals (cosalite, native Bi; Cos, Bi) (Luziyuan, LZY-47). (c) Sphalerite breccia replaced by pyrite (Py), galena and cosalite (Cos) (Luziyuan, LZY-47). Qz: quartz. (d) Grain of arsenopyrite (Asp) enclosed in sphalerite (Luziyuan, LZY-47). (e) Brecciation and replacement of sphalerite (Sp) by galena (Gn) and pyrite (Py) (Dabaoshan, DBS-2); (f) Brecciation and replacement of sphalerite by galena vein, and euhedral pyrite by sphalerite (Dabaoshan, DBS-2). (g) Stannite (Stn) associated with chalcopyrite (Cp) in arsenopyrite (Asp) (Laochang, LC-21). Ten: tennantite. (h) Banding textures in nodular sphalerite (Niujiaotang, L-13). (i) Coarse, massive sphalerite brecciation textures associated with small-scale recrystallisation of sphalerite and pyrite (Niujiaotang, H-22). (j) Nucleation of small greenockite grains (Grk; <1 μm) along fractures and at the margins of brecciated sphalerite (Niujiaotang, B-6). Inset shows sphalerite in the core of greenockite (Niujiaotang, B-6). (k) Sphalerite with porous margins and rims of pyrite (Jinding, JD-150). Gn: galena. (l) Sphalerite with minor marginal galena containing coarse inclusions of barite (Bar) (Jinding, JD-150).

which are enriched in Cu and Bi, and have higher fS_2 (pyrite stability field).

The samples analysed from *Dabaoshan* are from the largest orebody (number 1) and they all show extensive brecciation and replacement of sphalerite by galena and pyrite (Fig. 12e,f). However, replacement of galena by sphalerite is also seen (Fig. 11f), concordant with a protracted geological history as discussed above. The sphalerite has relatively constant and high Fe content (~12 wt.% Fe).

The sphalerite in the analysed samples from *Laochang* has high and relatively constant Fe content (~15 wt.%). The reduced character of the ore associations is also underlined by abundant pyrrhotite inclusions in pyrite (Fig. 11g). The ore also contains larger masses of recystallized

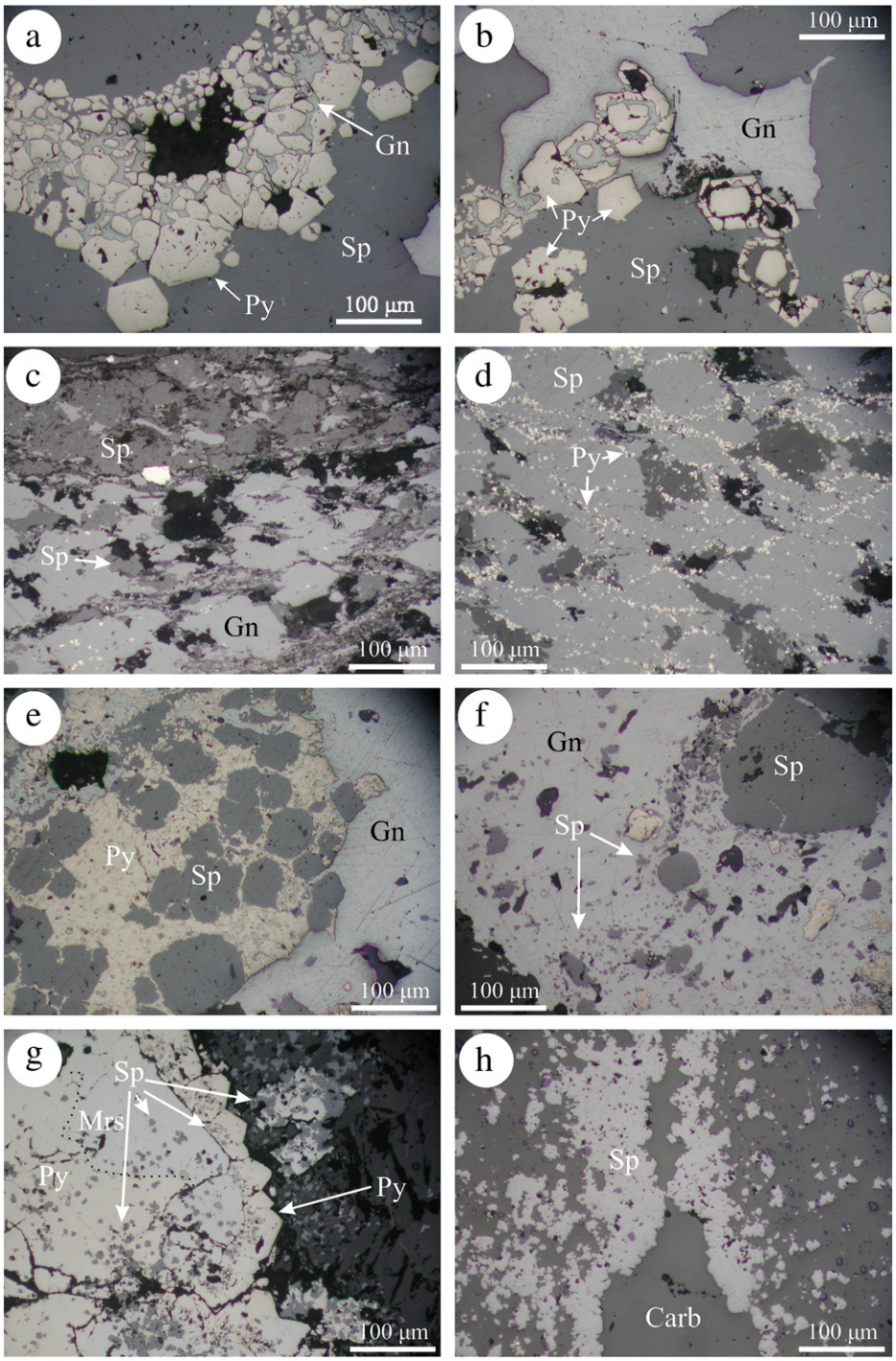

Fig. 13. Photomicrographs in reflected light illustrating textures and structures of Pb-Zn ores from Huize, Mengxing and Jinding. (a) Late small pyrite grains (Py) clustered along fringes or within areas spreading across galena (Gn) -sphalerite (Sp) boundaries (Huize, HZF-1062). (b) Atoll-like pyrite (Py) in sphalerite and galena (Huize, HZF-1062). (c) Brecciated galena and sphalerite occurring together and domains indicative of ductile deformation (Mengxing, M-11). (d) Small pyrite grains (Py), located along thin meshed veinlets, overgrow onto the sphalerite mass (Mengxing, M-11). (e) Pyrite-sphalerite assemblage with later galena (Mengxing, M-11); (f) Coarse sphalerite relics in galena and smaller, dusty sphalerite in the surrounding galena (Mengxing, M-11). (g) Small grains of sphalerite spread throughout the core and overgrowth zone of coarse pyrite, as well as into the carbonate gangue (Jinding, JD-148). The pyrite contains domains of marcasite (Mrs). (h) Small disseminated sphalerite occurs in the carbonate-dominant rock (Jinding, JD-91).

colloidal pyrite, some of them with orbicular texture and xenomorphic pyrite nucleated in the cores (Fig. 11h). Reworking of the ore is shown by extensive brecciation and also by replacement of pyrite by sphalerite, with associated remobilisation of minor galena and chalcopyrite along the replacement boundaries (Fig. 11i). Arsenic-bearing pyrite and arsenopyrite with inclusions of stannite are typical for the pyritic ore (Fig. 12g). This association contains abundant galena and is rich in Sb- and As–Pb and Cu-sulphosalts. The sulphosalts include minerals from the jordanite-geocronite, bournonite-seligmanite, tetrahedrite-tennantite series, dufrénoysite and gratonite, as identified by SEM-EDAX analysis by us (empirical compositional ranges: $Jord_{60}Geocron_{40}$ – $Jord_{62}Geocron_{38}$; $Bnn_{30}Slg_{70}$ – $Bnn_{78}Slg_{22}$; and $Tet_{58}Tenn_{42}$ –

Table 3
Summary of LA-ICMS data for sphalerite by deposit and sample (concentrations in ppm).

	Mn	Fe	Co	Ni	Cu	Ga	Ge	As	Se	Ag	Cd	In	Sn	Sb	Te	Au	Tl	Pb	Bi	U
Hetaoping																				
HTP-27																				
MEAN (8)	2832	37,201	110	–	9.7[a]	0.87	2.7	–	22.0	5.7	4240	0.01	0.11	1.9	–	–	–	3.5[a]	0.01	–
S.D.	16.8	2139	1.2	–	3.2	0.53	0.09	–	7.5	1.1	66.6	0.003	0.01	1.9	–	–	–	2.3	0.003	–
MIN	2818	32,878	108	–	6.8	0.33	2.6	–	11.6	4.5	4128	0.007	0.09	0.025	–	–	–	0.17	0.01	–
MAX	2866	39,021	112	0.05	16.4	1.8	2.8	–	32.3	8.0	4328	0.015	0.12	5.8	–	0.01	0.01	6.6	0.02	0.002
HTP-174																				
MEAN (8)	5115	100,274	78.3	–	1753[a]	0.16	3.0	–	16.5	12.7	5847	0.13	–	9.3	–	–	–	23.3[a]	0.53[a]	–
S.D.	544	7227	8.7	–	2881	0.14	0.19	–	8.6	6.7	504	0.03	–	7.3	–	–	–	23.6	0.35	–
MIN	4339	92,512	70.2	–	11.8	0.06	2.8	–	7.7	4.7	5420	0.09	–	0.27	–	–	–	0.88	0.02	–
MAX	5766	114,483	94.1	0.09	8337	0.46	3.3	–	33.4	25.2	6995	0.18	0.13	21.5	–	0.09	0.08	63.4	0.93	–
HTP-163																				
MEAN (8)	1273	20,849	449	0.22	104[a]	0.57	2.8	–	55.7[a]	6.4	4125	0.003	–	2.6	–	–	–	85.3[a]	3.2[a]	–
S.D	29.5	409	20.6	0.10	272	0.23	0.19	–	23.1	2.0	95.4	0.001	–	2.7	–	–	–	127	3.2	–
MIN	1241	20,311	428	0.15	5.7	0.32	2.5	–	25.4	4.4	3991	0.001	–	0.14	–	–	–	0.52	0.10	–
MAX	1325	21,367	473	0.47	778	0.87	3.1	–	85.9	10.1	4237	0.005	0.10	6.6	–	0.11	0.004	364	8.0	0.008
Luziyuan																				
LZY-47																				
MEAN (8)	1462	43,866	434	–	41.7[a]	0.32	2.9	–	117	4.6	2280	0.11	0.12	7.0	–	0.14	–	352[a]	14.8[a]	–
S.D.	297	667	12.5	–	64.0	0.29	0.19	–	12.3	1.2	68.0	0.004	0.06	8.1	–	0.15	–	630	17.8	–
MIN	1241	43,040	420	–	4.6	0.16	2.7	–	95.1	3.8	2168	0.11	0.03	0.30	–	0.02	–	0.61	2.3	–
MAX	2143	44,768	461	0.47	194	1.0	3.3	–	136	7.6	2393	0.12	0.24	26.1	–	0.47	0.16	1545	55.3	0.14
LZY-29																				
MEAN (8)	654	99,242	244	–	254[a]	0.56	3.1	–	1.5	8.6	1967	0.05	3.0	–	–[a]	–	–	15.4[a]	–[a]	–
S.D	41.0	4630	31.7	–	305	0.07	0.45	–	1.6	4.8	145	0.02	3.8	–	–	–	–	22.3	–	–
MIN	601	93,164	212	–	15.8	0.47	2.5	–	1.1	4.4	1688	0.01	0.04	–	–	–	–	0.58	–	–
MAX	737	105,858	313	1.2	873	0.67	3.7	4.7	2.6	17.2	2091	0.07	9.1	21.5	–	0.13	0.23	63.7	0.37	0.01
LZY-61																				
MEAN (8)	1093	57,305	411	0.30	13.8	0.12	3.0	–	16.1	4.7	2194	0.007	0.13	–	–	0.04	–	3.3	–	–
S.D	102	1690	2.4	0.04	3.9	0.01	0.09	–	3.2	0.36	82.9	0.002	0.03	–	–	0.03	–	2.6	–	–
MIN	996	55,373	406	0.24	8.4	0.11	2.9	–	12.2	4.2	2099	0.005	0.09	–	–	0.01	–	0.04	–	–
MAX	1270	60,554	413	0.35	20.1	0.16	3.2	0.41	21.5	5.4	2362	0.01	0.17	3.5	–	0.11	0.01	8.4	1.1	–
Dabaoshan																				
DBS-1																				
MEAN (10)	1762	110,336	0.19	–	155	38.6	3.1	–	–	21.9[a]	5580	122	5.5[a]	3.0	–	–	–	51.7[a]	–	–
S.D	457	3497	0.12	–	30.8	14.6	0.25	–	–	6.8	62.1	8.1	6.9	4.1	–	–	–	153	–	–
MIN	675	102,897	0.02	–	110	19. 9	2.8	–	–	12.5	5459	111	1.4	0.15	–	–	–	1.0	–	–
MAX	2171	114,283	0.41	0.20	191	65. 8	3.6	–	–	32.1	5650	132	24.2	11.1	–	0.07	0.08	487	0.91	2.3
DBS-2																				
MEAN (8)	2347	119,903	5.4	–	1418[a]	12.8	3.3	–	–	31.2[a]	5475	300	19.0[a]	2.2	–	–	–	14.9[a]	–	–
S.D	139	3574	0.84	–	1945	4.0	0.46	–	–	29.6	482	69.7	14.0	2.9	–	–	–	21.0	–	–
MIN	2067	113,228	4.3	–	228	8.0	2.6	–	–	9.3	4659	201	2.8	0.12	–	–	–	0.48	–	–
MAX	2475	125,179	6.6	0.37	5803	21.5	4.2	3.2	–	97.7	5882	415	46.0	8.5	–	–	0.06	49.4	–	–
DBS-6																				
MEAN (8)	2425	120,842	1.3	–	946[a]	33.9	3.5	–	–	54.7[a]	5779	285	13.1[a]	7.3	–	–	–	9.2[a]	–	–
S.D	189	4016	1.1	–	1048	27.4	0.10	–	–	61.4	146	23.9	14.7	8.3	–	–	–	16.4	–	–
MIN	2188	114,119	0.14	–	194	11.0	3.3	–	–	10.2	5547	260	2.1	0.17	–	–	–	0.70	–	–
MAX	2642	125,441	3. 7	0.11	3006	91.7	3.6	–	–	198	5951	336	46.8	19.0	–	–	0.14	49.0	–	–

Bainiuchang																				
BNC-3																				
MEAN (10)	3883	134,553	6.3	–	2254[a]	14.1	3.4	–	–	38.8[a]	8195	110	1129[a]	2.9	–	–	–	2.5	–	–
S.D	975	11,842	0.93	–	3042	5.4	0.56	–	–	48.4	278	84.2	968	2.8	–	–	–	1.2	–	–
MIN	2965	119,171	4.4	–	132	6.8	2.8	–	–	9.0	7744	35.1	37.8	0.29	–	–	–	0.72	–	–
MAX	6537	157,870	7.5	0.57	10,512	23.2	4.7	1.7	7.5	172	8564	262	2558	9.7	0.58	0.06	0.03	5.1	–	–
BNC-10 (8)																				
MEAN	3945	154,177	0.11	–	5702[a]	7.6	5.4	–	–	95.1[a]	5568	21.9	660[a]	8.3	–	–	–	18.3[a]	–	–
S.D	1073	10,154	0.11	–	3988	7.4	6.3	–	–	47.3	255	19.9	1091	6.6	–	–	–	21.0	–	–
MIN	2439	142,091	0.01	–	1283	2.2	2.0	–	–	46.9	5256	3.5	8.3	0.10	–	–	–	1.0	–	–
MAX	5782	171,476	0.31	–	11,261	24.3	20. 8	–	13.9	188	5876	49.4	3097	17.9	0.47	–	–	64.6	–	–
Laochang																				
LC-9																				
MEAN (14)	2734	128,199	0.43	–	180[a]	15. 9	3.7	–	–	6.4	8673	183	5.7	–	–	–	–	43.1[a]	–	–
S.D	79.4	2172	0.26	–	64.5	13.6	1.4	–	–	1.0	142	37.8	3.1	–	–	–	–	148	–	–
MIN	2626	123,724	0.07	–	119	5.6	2.1	–	–	4.8	8420	80.4	2.4	–	–	–	–	0.30	–	–
MAX	2879	132,072	0.91	0.39	380	46.5	7.1	4.1	4.0	8.6	8939	232	13.6	4.1	–	–	1.4	556	0.05	–
LC-19																				
MEAN (8)	3465	142,095	0.58	–	251	41.2	3. 7	–[a]	2.2	6.3	8769	293	10.3[a]	–	–	–	–	1.7[a]	–	–
S.D	320	5247	0.39	–	61.8	37.6	0.33	–	0.70	0.66	203	111	12.5	–	–	–	–	1.5	–	–
MIN	3123	138,823	0.18	–	164	5.7	3.2	–	1.3	5.2	8306	236	2.2	–	–	–	–	0.36	–	–
MAX	4111	154,203	1.2	0.08	364	117	4.3	36.4	3.1	7.5	8947	566	38.1	1.5	–	–	0.84	4.8	0.02	0.39
LC-18																				
MEAN (8)	3225	124,117	2.0	0.31	436[a]	17.5	5.4	2.6	–	8.0	8825	138	6.0	1.6	–	–	0.68	18.6[a]	0.008	–
S.D	63.5	2510	1.2	0.55	646	9.5	4.5	3.6	–	1.4	376	56.3	1.9	1.0	–	–	0.80	16.8	0.002	–
MIN	3114	121,694	0.44	0.07	128	2.3	2.7	0.002	–	5.8	8519	65.5	3.8	0.40	–	–	0.10	2.8	0.006	–
MAX	3309	128,675	4.4	1.7	2020	24.5	15.1	10.3	1.32	10.1	9600	231	8.3	2.9	0.07	–	2.6	54.1	0.01	0.002
Huize																				
HZF-1086																				
MEAN (8)	111	34,315	0.04	0.16	602[a]	5.0	165	18.6	–	28.8[a]	3059	–	0.11	64.0[a]	–	–	0.04	13.0[a]	0.01	0.000
S.D	19.0	7103	0.01	0.07	338	6. 7	90.5	30.2	–	21.2	897	–	0.02	102	–	–	0.05	14.2	0.004	0.001
MIN	87.5	25,183	0.03	0.04	263	0.06	80.2	0.23	–	13.3	1728	–	0.08	0.37	–	–	0.004	1.2	0.009	0.000
MAX	137	47,248	0.05	0.24	1188	19.8	354	89.7	1.6	76.8	4647	0.003	0.14	306	0.05	–	0.17	44.3	0.02	0.001
HZF-1062																				
MEAN (8)	58.8	13,760	–	–	157[a]	0.81	52.3	–	–	28.5	1689	–	0.81	17.5[a]	–	–	0.16	13.1[a]	0.01	–
S.D	47.1	13,135	–	–	189	0.91	71.8	–	–	14.5	529	–	0.76	45.5	–	–	0.28	22.5	0.003	–
MIN	7.1	4873	–	–	7.2	0.05	2.7	–	–	9.6	894	–	0.07	0.03	–	–	0.000	0.55	0.006	–
MAX	125	43,664	0.04	0.03	533	2.7	199	109	0.72	50.7	2474	0.46	2.1	130	–	–	0.83	67.7	0.02	0.02
HZF-1065																				
MEAN (8)	119	15,552	0.02	–	102[a]	6.0	29.9	–	–	10.8 [a]	1612	1.9	4.1[a]	4.7[a]	–	–	–	3.7[a]	0.009	–
S.D	111	6211	0.02	–	173	7.1	51.7	–	–	3.5	114	1.9	9. 5	9.2	–	–	–	4.1	0.002	–
MIN	11.2	6482	0.002	–	7.0	0.17	2.8	–	–	6.0	1423	0.34	0.16	0.06	–	–	–	0.43	0.007	–
MAX	300	24,444	0.06	0.10	521	21.1	154	385	0.81	16.8	1764	5.6	27.4	27.4	–	–	0.20	12.4	0.01	–
Niujiaotang																				
B-10																				
MEAN (10)	9.1[a]	13,781	–	–	–	9.8	44.3	–	0.70	20.4	13,963	0.18	1.6	–	–	–	0.60	395[a]	0.06	–
S.D	7.6	22,866	–	–	–	10.5	43.2	–	0.27	23.0	8007	0.26	1.9	–	–	–	0.28	733	0.06	–
MIN	2.1	985	–	–	–	0.02	2.15	–	0.31	3.5	4226	0.001	0.14	–	–	–	0.15	27.5	0.03	–
MAX	24.0	77,235	1.4	6.2	196	32.5	127	7.1	1.2	75.4	26,998	0.75	5.8	0.50	–	–	0.88	2427	0.22	0.45
B-6																				
MEAN (8)	6.0	7461	–	–	14.4	7.8	29.7	–	0.35	5.6	9000	0.05	0.74[a]	–	–	–	0.41	211[a]	0.02	–
S.D	5.6	8322	–	–	11.6	4.1	18.9	–	0.12	1.6	2363	0.06	0.37	–	–	–	0.28	225	0.009	–
MIN	0.63	1033	–	–	2.7	2.5	6.5	–	0.16	3.8	6334	0.003	0.18	–	–	–	0.06	43.5	0.01	–
MAX	17.3	23,399	0.35	0.48	38.1	12.9	59.4	0.97	0.53	8.1	13,439	0.19	1.2	0.40	–	–	0.89	673	0.04	0.006

(continued on next page)

Table 3 (*continued*)

	Mn	Fe	Co	Ni	Cu	Ga	Ge	As	Se	Ag	Cd	In	Sn	Sb	Te	Au	Tl	Pb	Bi	U
Niujiaotang																				
H-22																				
MEAN (8)	75.7	13,857	–	–	124	16.1	182	–	0.43	5.0	7028	0.034	2.4	–	–	–	12.1	835[a]	0.02	–
S.D	93.3	12,858	–	–	113	25.3	171	–	0.15	1.6	4553	0.067	4.3	–	–	–	14.2	1152	0.004	–
MIN	4.3	2192	–	–	0.62	0.87	16.8	–	0.16	3.7	956	0.000	0.09	–	–	–	1.6	126	0.02	–
MAX	225	36,604	2.1	0.03	302	64.5	546	11.0	0.67	8.3	15,212	0.193	12.3	1.4	–	–	43.6	3493	0.03	–
Mengxing																				
M-1																				
MEAN (10)	40.1	9072	0.82	–	156[a]	3.3	26.8[a]	127[a]	–	4.3	9465	–	0.27	87.9	–	–	8.8	972	0.07	–
S.D	51.5	2736	0.76	–	31.5	1.8	18.0	168	–	0.34	2083	–	0.13	32.7	–	–	4.9	1070	0.08	–
MIN	6.9	6556	0.06	–	111	1.4	4.3	16.6	–	4.0	7048	–	0.10	44.9	–	–	3.6	160	0.01	–
MAX	168	14,789	2.4	37.8	201	7.1	56.7	578	1.1	5.1	12,745	0.04	0.46	158	1.1	–	18.1	3031	0.27	0.05
M-11																				
MEAN (8)	281[a]	656[a]	4.3	–	4.4	0.83	2.8	5.9[a]	0.61	4.2	15,472	–	0.12	1.9	–	–	8.6	386	0.06	0.15
S.D	500	1159	5.2	–	1.7	0.91	0.39	10. 6	0.21	0.3	1032	–	0.05	1.1	–	–	2.8	84.4	0.03	0.15
MIN	11.9	79.2	1.9	–	1.8	0.22	2.3	0.15	0.36	3.8	13,875	–	0.09	0.54	–	–	5.1	326	0.03	0.003
MAX	1451	3477	17.0	3.3	6.9	3.0	3.3	31.7	0.90	4.8	16,560	0.005	0.24	3.4	–	–	12.4	586	0.12	0.37
Jinding																				
M																				
MEAN (8)	538[a]	581	17.8[a]	0.64	5.6	0.96	8.8	18. 6	–	30.4	6561	–	–	2.0	–	–	17.3	483[a]	–	0.32
S.D	632	261	5.6	0.27	1.3	0.38	1.7	10.0	–	11.7	1621	–	–	0.86	–	–	4.5	292	–	0.17
MIN	52.2	300	8.6	0.37	3.8	0.58	6.9	8.6	–	17.4	4106	–	–	1.4	–	–	11.6	211	–	0.06
MAX	1937	1120	25.6	1.3	7.7	1.7	12.1	34. 5	3.7	52.5	9683	–	0.30	3.8	–	–	23.9	1099	–	0.55
Jind-150																				
MEAN (8)	124[a]	1733[a]	3.6	–	1406[a]	3.4	3.4	26.0	–	49.8	9037	–	–	4.9	–	–	12.6[a]	4145[a]	–	–
S.D	72.9	1009	2.1	–	926	2.8	1. 7	26.6	–	40.9	9158	–	–	2.4	–	–	6.1	4624	–	–
MIN	10.6	206	0.73	–	31.0	0.37	1.8	2.2	–	4.9	187	–	–	2.6	–	–	2.1	247	–	–
MAX	212	3105	6.8	5.7	2798	7.2	7.2	84.7	–	136	23,075	–	12.3	10.3	–	–	22.1	12,955	–	–
Jind-148																				
MEAN (8)	62.3[a]	670	–	–	–	1.3	20. 8	–	–	4.0	35,468	–	–	–	–	–	6.7[a]	159[a]	–	–
S.D	111	947	–	–	–	0.67	25.4	–	–	0.68	24,028	–	–	–	–	–	4.7	113	–	–
MIN	1.1	52.8	–	–	–	0.38	3.9	–	–	3.4	1279	–	–	–	–	–	2.0	53.9	–	–
MAX	309	2624	–	–	–	2.0	75.1	–	–	5.6	68,552	1.4	–	–	–	–	12.9	338	–	–
Jind-155-26																				
MEAN (8)	11.7[a]	2309	0.33	–	97.9[a]	4.4[a]	12.4	60.9[a]	0.50	4.4	20,692	0.006	0.23	46.3	–	–	21.3[a]	913[a]	0.04	–
S.D	11.6	792	0.34	–	28.9	3.2	17.9	81.0	0.16	0.89	8949	0.006	0.14	47.8	–	–	22.2	1240	0.009	–
MIN	0.86	1296	0.02	–	33.4	0.41	3.1	12.9	0.33	3.8	6592	0.002	0.13	15.3	–	–	4.3	145	0.03	–
MAX	33.6	3625	1.11	0.33	122	10.9	56.3	257	0.78	6.3	35,684	0.02	0.55	159	–	–	73.3	3931	0.05	–

[a] Indicates the mean includes at least one spot in which the element in question appears as inclusions on the LA-ICPMS profile; The number in bracket is the number of individual spot analyses.

Tet_2Tenn_{98}). Such assemblages are very common in remobilised ores from many Caledonian VMS and SEDEX deposits (e.g., Sulitjelma, Bleikvassli; Norway; Cook, 1996; Cook et al., 1998).

The samples from *Bainiuchang* were collected along the strike of the same orebody (Duimenshan) at ~150 m distance from one another. The sphalerite has relatively constant and high Fe values (~17 wt.%) and contains micron-scale inclusions of chalcopyrite (Fig. 11j,k). The sulphide ore contains early galena replaced by sphalerite and mildly brecciated pyrite/pyrrhotite (replaced by marcasite) and crosscut by late pyrite veinlets (Fig. 11l).

Our samples from *Huize* were collected from two sections (a section is some 50 m long) at the same level (1764 m), at intermediate depth of the orebody VI in the Qilinchang deposit. The two that are in the same section (8) are some 10 m apart whereas the one from Section 12 is some 200 m apart from the ones in Section 8. The Fe content in sphalerite from these samples is low (from <1 to ~4 wt.%), where the higher Fe content is found in the sample from Section 12 (HFZ-1086). Sphalerite is associated with galena and intimately intergrown with pyrite; the latter occurs as small grains clustered along fringes or within areas spreading across galena–sphalerite boundaries (Fig. 13a). This pyrite characteristically appears to be part of an aggregate composed of 'pieces' that can be recognised as the result of milling, corrosion or mild brecciation, except that some of the marginal grains – larger in size – tend to be idiomorphic. However, the textures suggest that all three sulphides may have formed at the same time from an 'emulsion-like' precipitate, a feature that is typical of seafloor/basinal style of mineralisation. In detail some of the pyrite has an atoll-like morphology (Fig. 13b) resembling key textures known from VMS deposits. Pyrite is, however, replaced by galena and to a lesser extent also by sphalerite, suggesting post-depositional evolution of the ore.

The samples from *Niujiaotang* analysed here are collected from two mining levels of the same orebody (IIb); samples B-6 and B-10 are from a location adjacent to one of the marginal faults, some 300 m apart from one another. Sample H-22 is from an 80 m deeper level (650 m) from the middle of the lens. The Fe content of sphalerite is relatively low (from <1 to 3 wt.%), but highly variable (some areas can be up to 7 wt.%) within each sample and from one sample to another. This variation correlates with the colour zonation noted in hand specimens but which could not be satisfactorily imaged by SEM. Banding textures in nodular sphalerite are marked by grain size (Fig. 12h) and in the coarse, massive sphalerite brecciation textures are typical, accompanied by small-scale recrystallisation of sphalerite; minor pyrite is also seen within such areas (Fig. 12i). Cadmium enrichment is seen as nucleation of small greenockite grains (<1 μm) along fractures and at the margins of brecciated sphalerite (Fig. 12j). In detail such greenockite grains have cores of sphalerite (Fig. 12j inset).

Our samples from *Mengxing* come from the central part of one of the largest orebodies (no. III) and were collected from the same mining level (920 m), at a distance of some 200 m from one another. The sphalerite has a low Fe content (from <1 to 1.5 wt.%), among the lowest in the present suite of samples. Galena and sphalerite occur together in the massive ore and are often brecciated, showing domains with a ductile deformational character (Fig. 13c). Small pyrite grains, along thin, meshed veinlets, overgrow onto the sphalerite mass (Fig. 13d). As in Huize, the relationships between the sulphides also show that some galena is later than the pyrite-sphalerite association (Fig. 13e). Although larger grains of sphalerite may represent relics, the surrounding galena contains smaller, dusty sphalerite grains (Fig. 13f) that, in our opinion, possibly post-date the galena rather than represent replacement relics.

The samples from *Jinding* studied here are from different levels of the three oreblocks mentioned above and from different types of ores (Table 2). The Fe content is variable but low (<1.0 wt.%), the lowest in the present sample suite. The pyrite-marcasite rich ore show coarse cores with overgrowths of the same minerals and strong brecciation; sphalerite is present as small grains spread throughout the core-overgrowth, as well as into the carbonate gangue (Fig. 13g). In the carbonate rocks, sphalerite occurs as small disseminated grains but increases in abundance toward the margins of fractures (Fig. 13h). In the sandstone, sphalerite, galena and pyrite occur interstitial to quartz grains but occasionally also forms larger patches. In this case, the margins of sphalerite contain galena (Fig. 12k) and/or pyrite, and the sphalerite cores contain coarse inclusions of barite (Fig. 12l). The latter indicate precipitation from high-salinity brines concordant with fluid inclusion studies in sphalerite (Xue et al., 2007a).

5. Approach and experimental methods

The samples selected for LA-ICPMS analysis (Table 2) were biased towards coarse-grained sphalerite generally free of visible inclusions; one-inch polished mounts were prepared from each. Scanning electron microscopy in backscattered electron mode was used to characterise the samples, paying particular attention to compositional inhomogeneity, mineral inclusions, zoning, or other textural aspects, all of which may impact upon trace element distributions. Each specimen was also studied by electron microprobe to ascertain the Zn content, which would be used as the internal standard.

LA-ICPMS analysis of sphalerite was made using the Agilent HP-7700 Quadripole ICPMS instrument at CODES (University of Tasmania, Hobart, Australia). The instrument is equipped with a high-performance New Wave UP-213 Nd:YAG Q-switched laser ablation system equipped with MeoLaser 213 software. We have followed the procedure and operating conditions outlined by and previously applied to sphalerite by Cook et al. (2009).

Pre-defined areas of the polished blocks were ablated. We used a consistent 50 μm diameter spot size for all 231 analyses. Each analysis was performed in the time-resolved mode, which involves sequential peak hopping through the mass spectrum. The laser system was operated at a consistent 10 Hz pulse rate; laser energy was typically 5–6 Jcm^{-2}. At these conditions, each pulse removes ~0.3 μm of the samples, resulting in an ablation rate of 3.0 μm/s. The following isotopes were monitored: ^{49}Ti, ^{51}V, ^{53}Cr, ^{55}Mn, ^{57}Fe, ^{59}Co, ^{60}Ni, ^{65}Cu, ^{66}Zn, ^{69}Ga, ^{72}Ge, ^{75}As, ^{77}Se, ^{93}Nb, ^{95}Mo, ^{107}Ag, ^{111}Cd, ^{115}In, ^{118}Sn, ^{121}Sb, ^{125}Te, ^{182}W, ^{185}Re, ^{197}Au, ^{205}Tl, ^{208}Pb ^{209}Bi and ^{238}U. Analysis time for each sample was 90 s (30-second measurement of background with laser off, and a 60-second analysis with laser-on. Acquisition time for all masses was set to 0.02 s, with a total sweep time of ~0.6 s. Data reduction was undertaken using Zn as the internal standard.

Calibration was performed using the in-house standard (STDGL2b-2), comprising powdered sulphides doped with certified element solutions and fused to a lithium borate glass disc. This standard is suitable for quantitative analyses in different sulphide matrixes (Danyushevsky et al., 2011). Empirical correction factors (Danyushevsky et al., 2011) were applied to the measured ppm values in each analysis as follows: Mn 1.46, Fe 1.49, Co 1.51, Ni 1.59, Cu 1.53, Ga 1.45, As 1.36, Se 1.85, Mo1.62, Ag 1.40, Cd 1.50, In 1.45, Sn 1.6, Sb 1.17, Te 1.00, Au 1.40, Tl 2.17, Pb 1.37, and Bi 1.33. These correction factors have been established by analysing sphalerite secondary standards using STDGL2b2 and reflect the significant elemental fractionation between Zn and the other elements during ablation. The error on the correction factors is <5%. Analytical accuracy is expected to be better than 20%.

Low Ge concentrations cannot be quantified with full confidence because the isotope weight of 72 is equal to $^{40}Ar^{32}S$ (and also $^{40}Ar^{32}O$ in the standard), and the Ge concentration in the standard is not high enough to ignore these interferences. For this reason, there is uncertainty concerning exactly how much Ge is in the standard and no Ge value is published for STDGL2b2 (Danyushevsky et al., 2011). Higher Ge values (those exceeding 20–30 ppm) can, however, be confidently compared with one another and are included in our datasets.

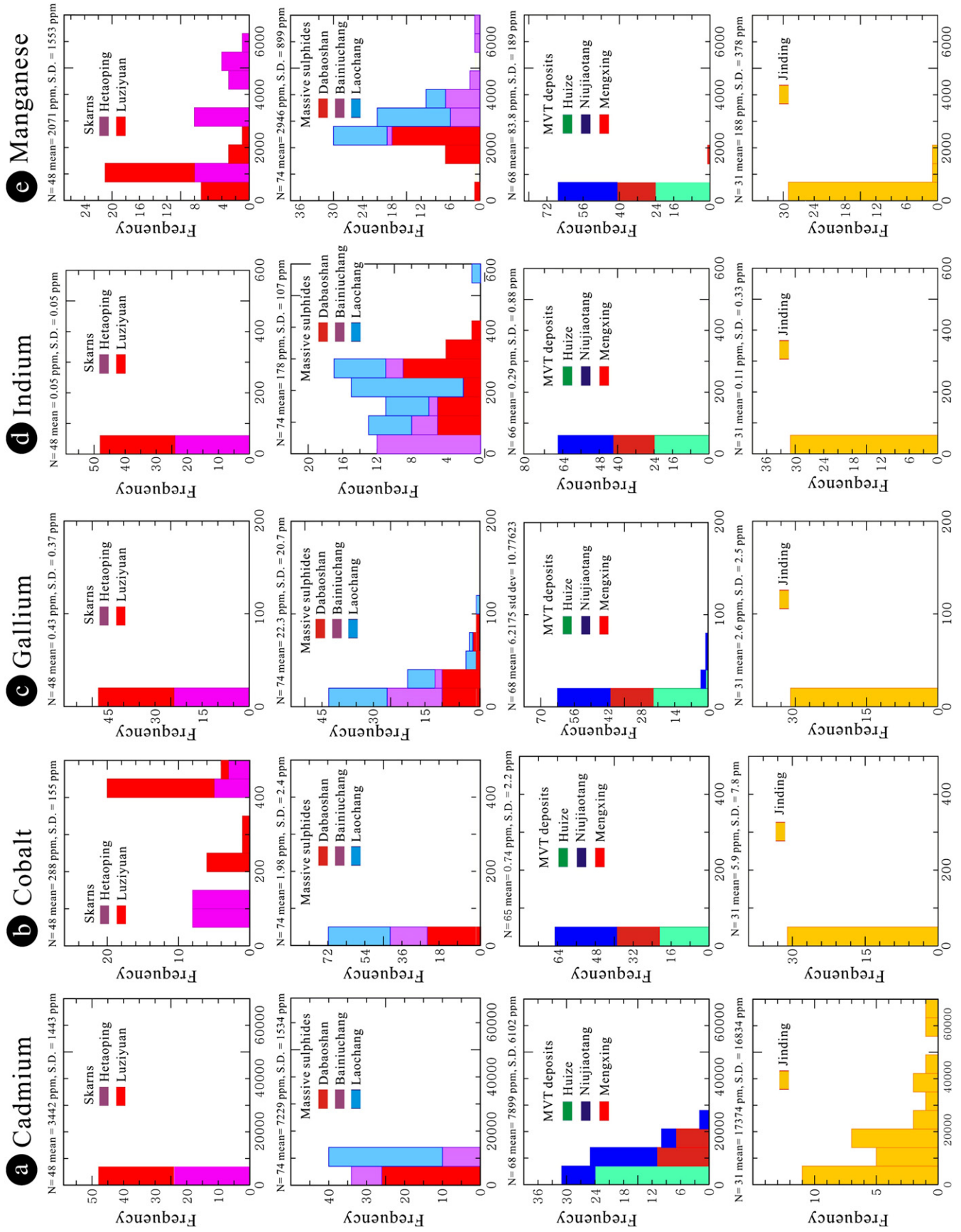

Fig. 14. Histograms showing the variation in (a) Cd, (b) Co, (c) Ga, (d) In, and (e) Mn in sphalerite from Pb–Zn deposits in South China.

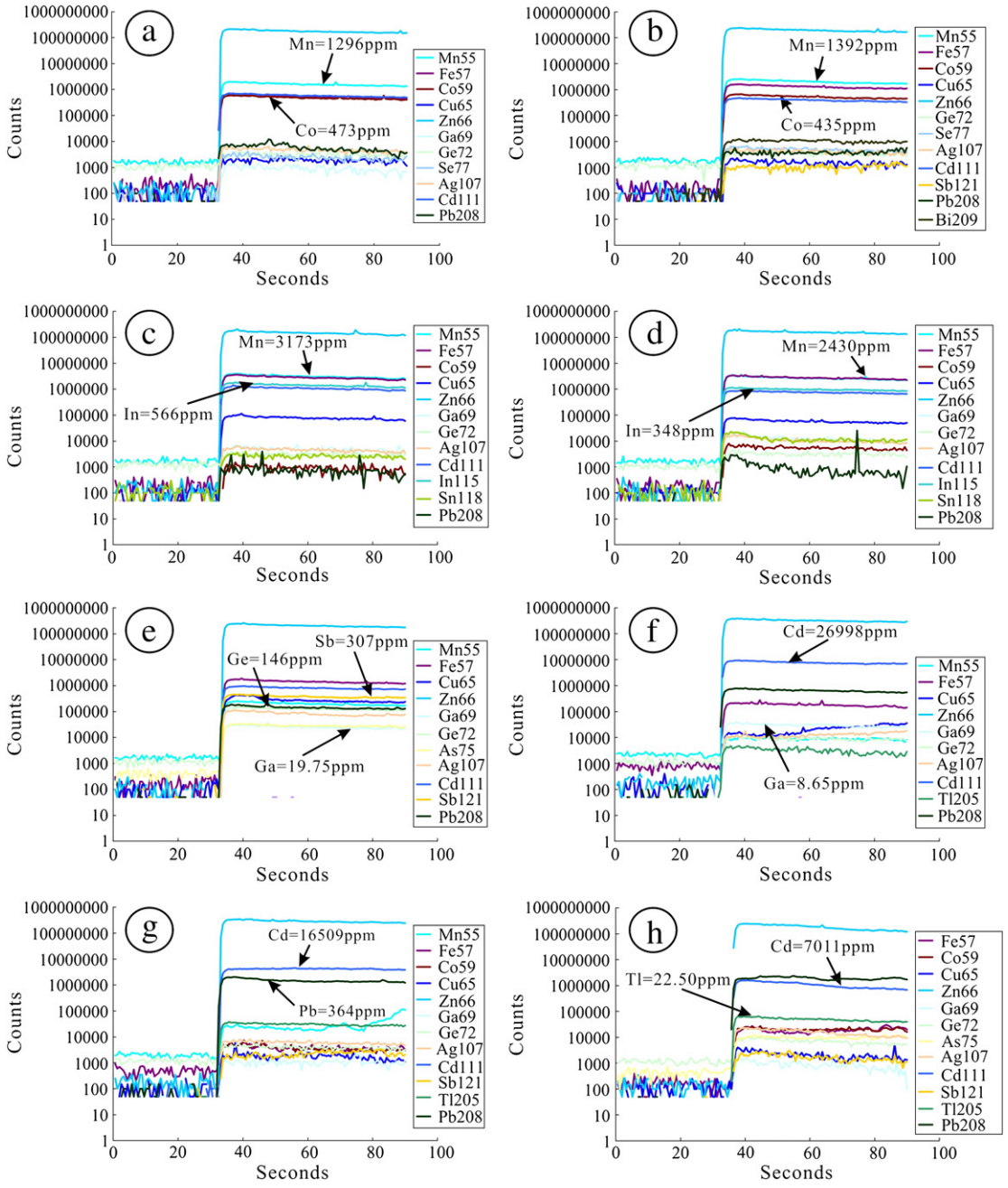

Fig. 15. Representative time-resolved depth profiles for sphalerite analysed in this study showing flat spectra indicative of solid solution; see text for additional explanation. (a) Hetaoping, HTP-63. (b) Luziyuan, ZLY-47. (c) Dabaoshan, DBS-2. (d) Laochang, LC-19. (e) Huize, HZF-1086. (f) Niujiaotang, B10. (g) Mengxing, M-11. (h) Jinding, JD-91.

The raw analytical data for each spot analysis is plotted as a line graph and the integration times for background and sample signal selected. The counts are then corrected for instrument drift (standards were run each 1½ to 2 h) and converted to concentration values using known values of Zn in the analyzed sphalerite as an internal standard. Based on the measured concentrations, detection limits were calculated for each element in each spot analysis (Electronic Appendix). These values are similar throughout the dataset since the consistent spot size has let to comparable count rates for each spot. The error on the element signal is calculated as $(\sigma/\sqrt{n})\times 100$, where σ is the standard deviation and n the number of data points across the selected signal interval. Total analytical error (precision) is expressed as a percentage of concentration and is an expression of analytical noise. The smooth profile, and good precision, observed for almost all analyses indicates the specimens to be homogeneous. In the subsequent section, we refer to mean analyses for a given element in sphalerite from a specific sample; these are simple numerical means of *n* individual analyses.

6. Results

The data are summarised, in Table 3, with means, standard deviations, maxima and minima for each sample. The ranges in absolute concentrations for selected elements are shown as histograms in Fig. 14. Representative time-resolved depth profiles are given in Fig. 15. Complete LA-ICPMS datasets can be found in Electronic Appendix A.

All samples contain measurable quantities of *silver*. A remarkable feature of the dataset for Ag is that concentrations of the element are relatively constant (low standard deviations relative to mean) in each sample, but with some variation, often as much as an order of

magnitude between samples from a given deposit. The highest Ag concentrations are observed in Bainiuchang and Dabaoshan (deposit means 64 and 35 ppm, respectively). Interestingly, the two skarns have the lowest deposit means in the dataset (6.0 and 8.3 ppm for Luziyuan and Hetaoping, respectively). The Ag distribution in the Jinding samples illustrates the narrow variation within a sample but the broader variation between samples: means are 4.0 ± 0.7, 4.4 ± 0.9, 30.4 ± 11.7 and 49.8 ± 40.9 in samples JD148, 155–26, 0091 and Jind150, respectively.

Time-resolved depth profiles for *arsenic* are rarely flat. All concentrations above a couple of ppm are attributable to inclusions of As-bearing minerals. These are particularly abundant in the samples from Huize, Mengxing and Jinding and appear, from the profiles, to be of sizes extending down to the nanoscale. There is little evidence for any significant solid solution As in any of the samples studied, except for possibly some spots from Hui-1086 which had flat profiles (concentrations of a few tens of ppm As) although other spots in the same sample carried inclusions.

Bismuth is always <1 ppm (generally <0.1 ppm) in sphalerite except in the skarn samples, where a few individual spots give values up to 55 ppm (Luziyuan). In such cases, the time-resolved depth profiles show the presence of Bi–Pb–Cu-bearing mineral inclusions.

Cadmium concentrations also typically form a narrow cluster within sub-populations for specific samples, but with some modest variation from sample to sample. This is especially evident in the massive sulphide deposits, e.g., Dabaoshan, where mean concentrations in the 3 samples are 5779 ± 146, 5580 ± 62 and 5475 ± 482 ppm, and in the skarns, e.g., Hetaoping, where mean concentrations in the 3 samples are 4240 ± 67, 5847 ± 504 and 4125 ± 95 ppm. The MVT deposits, however, represent an exception to this rule due to the markedly different Cd concentrations in sphalerite of different types. This is best shown by Mengxing, where darker, higher-Fe sphalerite is lower in Cd (7000–12,700 ppm) than the pale, low-Fe variety (mean 15,718 ± 1048 ppm; Fig. 15g). The pattern at Niujiaotang is less clear with high Cd noted in sphalerite (Fig. 15f) with variable Fe contents, not only in the yellow sphalerite which is believed to be richer in Cd. Huize has some of the lowest Cd concentrations: ~3060 ppm in black sphalerite (Hui-1086) and 1610–1690 ppm in yellow sphalerite (HZF-1062 and -1065). The Jinding samples also show an unusually large variation from spot to spot with individual analyses as much as 6.5 wt.% Cd. Highest values are in the very-low-Fe sphalerite in JD-148. Cadmium distributions are summarised in a histogram (Fig. 14a).

Cobalt values are typically <1 ppm in all MVT and massive sulphide samples and Jinding, except for slightly elevated and consistent mean concentrations of 6.3, 5.4 and 18 ppm in samples Bainiuchang BNC3 Dabaoshan DBS2 and Jinding 0091, respectively. The skarn sphalerites are enriched in Co at concentrations one to two orders of magnitude higher than in other deposit types (Fig. 15a,b). These sub-populations show remarkable consistency within sphalerite from the same sample and restricted variation between samples from the same deposit: 110 ± 1.0, 78 ± 9.0 and 449 ± 21.0 ppm for the 3 samples from Hetaoping; 434 ± 12.0, 244 ± 32.0 and 411 ± 2.0 ppm for the 3 samples from Luziyuan. Cobalt distributions are summarised in a histogram (Fig. 14b).

Measured *copper* concentration sub-populations can be broadly divided into three main groups. Firstly, samples in which concentrations are low to very low (Mengxing M-11, Hetaoping HTP-27 and -163, Luziyuan LZY61 and the majority of the data from Niujiaotang and Jinding). The second group features erratic values, often up to several thousands of ppm, which can be directly related to widespread chalcopyrite inclusions (chalcopyrite disease). Although not restricted to these samples, chalcopyrite disease is particularly abundant in all the Bainiuchang samples and sample HTP174 from Hetaoping. The third and most interesting group are the consistent concentrations (typically 100–200 ppm) in Dabaoshan and Laochang sphalerite which correlate well with In content and are in the same range. We also observe relatively constant Cu concentrations in Mengxing M1, Jinding 155–26 and some spots from Huize, where moderate Cu (50–150 ppm) correlates with similar concentrations of Sb.

Iron concentration in the skarn sphalerite is typically constant within a given sample, but can vary significantly from sample to sample (2.1, 3.7 and 10.0 wt.% in the 3 samples from Hetaoping; 4.4, 5.7 and 9.9 wt.% in the 3 samples from Luziyuan. Inter-sample variation is much less in the massive sulphide sphalerites — all have Fe contents of ~11–15 wt.%. There is a large variation (from ~0.2 up to ~7 wt.%) in the Fe content of Niujiaotang sphalerite, reflecting the compositional differences between yellow and black sphalerite noted above. Similar absolute values and patterns are observed in the Mengxing population, with the pale yellow sphalerite (sample M-11) characterised by low Fe (80–3500 ppm) and darker sphalerite containing up to 1.5 wt.% Fe. There is also variation in the Huize population, though without the lowest values; sample 1086 has the highest Fe content (mean 3.4 wt.%). Jinding sphalerites are exceptionally low in Fe (as low as 50 ppm), with a deposit mean of 1344 ppm.

Gallium concentrations are <2 ppm in sphalerite from the skarn deposits and a maximum of 7, 11 and 21 ppm in Mengxing, Jinding and Huize (Fig. 15e), respectively. Significantly higher concentrations are observed in sphalerite from Niujiaotang (up to 65 ppm; Fig. 15f), albeit with variation from spot to spot (mean for the deposit: 11 ppm). Sphalerite in all the massive sulphide deposits is Ga-enriched — mean 11 ppm in Bainiuchang, 23 ppm in Laochang and 29 ppm in Dabaoshan, although all three deposits show a spread in the Ga value of individual spots from a few ppm up to 100 ppm. Gallium distributions are summarised in a histogram (Fig. 14c).

Given the analytical problems associated with quantification of *germanium* concentrations (see above), we cannot reliably give absolute values for this element. Deposits other than the 3 MVT deposits (except from a handful of values from Jinding JD148 giving a few tens of ppm) have Ge concentrations in sphalerite within the same range as interference from $^{40}Ar^{32}S$, and can thus be considered negligible. Measured concentrations in the MVT deposits, especially Huize and Niujiaotang, are distinctly higher, with individual values exceeding 300 ppm (Fig. 15e). There is, however, a marked variation from spot to spot, even if the time-resolved depth profiles are universally flat, and some samples, e.g., M-11 (Mengxing) contain no Ge.

Indium concentrations in sphalerite from all the MVT deposits, skarns and in Jinding are at or below the minimum detection limit, except for three spots from Huize (1.8, 3.6 and 5.6 ppm). In contrast, the three massive sulphide deposits are conspicuously enriched in indium. Similarly to Ga, Bainiuchang has the lowest mean concentration (71 ppm) and a marked variation within the samples (data range 4–262 ppm). Indium concentrations in Laochang sphalerite (mean 200 ppm; Fig. 15c) are more constant within each sample and are statistically close to identical in the three samples. Samples DBS2 (Fig. 15d) and DBS6 from Dabaoshan have identical concentrations and narrow standard deviations (300 ± 70 and 285 ± 24 ppm, respectively); concentrations in the third sample (DBS1) are somewhat lower (mean 122 ± 8 ppm). Indium distributions are summarised in a histogram (Fig. 14d).

All sphalerites contain measurable concentrations of *manganese*. Values in the MVT deposits and Jinding were, on average, <200 ppm, but typically with great variation both within and between samples (1–250 ppm). In the skarns and VMS/SEDEX deposits, however, concentrations were two-three orders of magnitude higher and remarkably constant among spots in a given sample (Fig. 15a,b). In Hetaoping, there is a direct correlation between Mn and Fe content in the three samples, in which the Mn/Fe ratio is preserved (0.05–0.07). Mean Mn concentrations in sphalerite from the three samples are 1273, 2832 and 5115 ppm. Similar variation in average concentration between samples is observed from the 3 samples from Luziyuan, albeit at somewhat lower concentrations (means 654, 1093 and 1462 ppm). Here, however, there is an inverse correlation between Mn and Fe, with the highest Mn-sphalerite having the lowest Fe

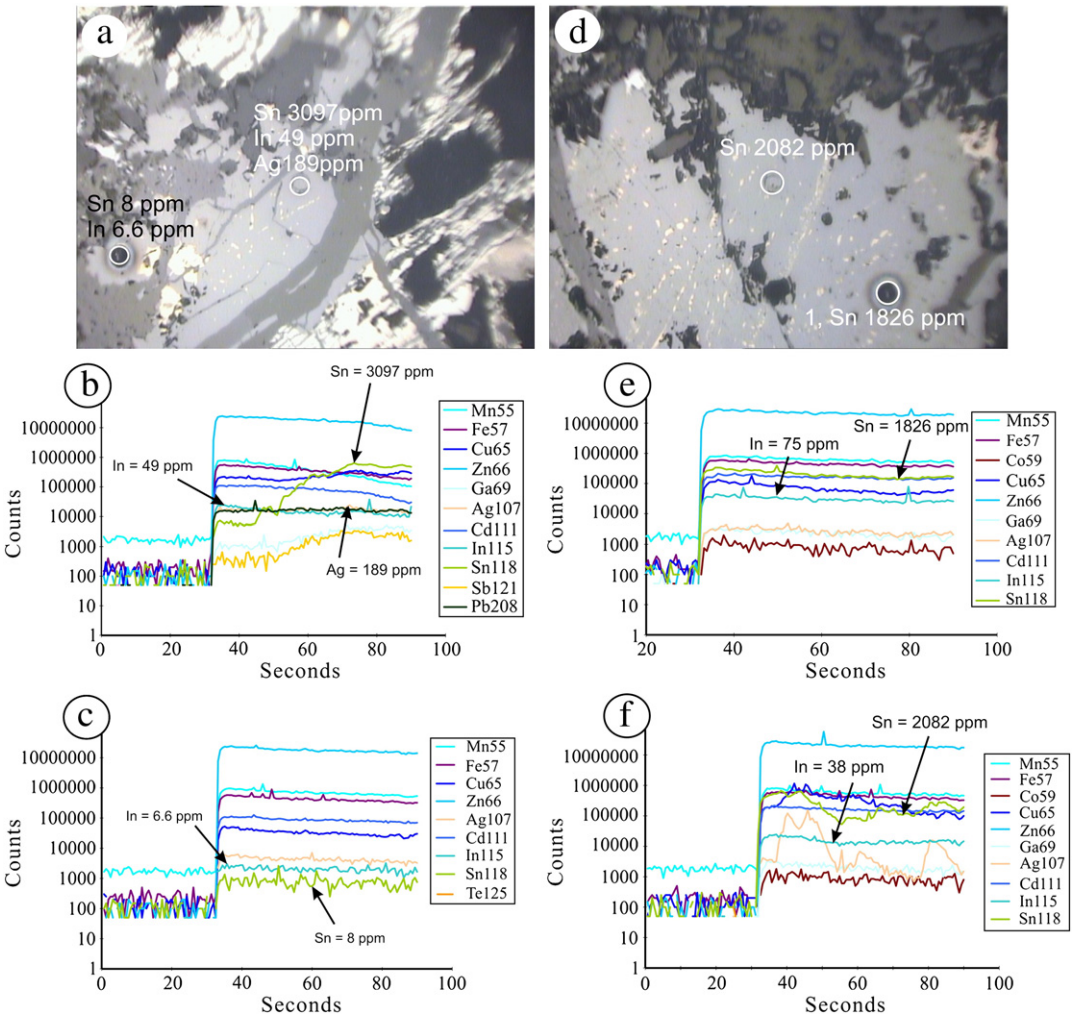

Fig. 16. Photographs and time-resolved LA-ICPMS depth profiles illustrating inclusion- and lattice-bound Sn in sphalerite from Bainiuchang. (a–c) Sample 3BNC; (d–f) sample 10BNC. See text for additional explanation.

content. The mean Mn/Fe ratios thus differ greatly from sample to sample. Comparably constant concentrations are also seen across the dataset for the VMS/SEDEX deposits (Fig. 15c,d), although in all three cases with less variation between samples from the same deposit than in the skarns, similar to that observed for Fe. Mean Mn concentrations in sphalerite from Bainiuchang, Laochang and Dabaoshan are 3910, 3059 and 2145 ppm, respectively. Manganese distributions are summarised in a histogram (Fig. 14e).

None of the analysed samples had sphalerite with significant concentrations of *molybdenum*. Inclusions of molybdenite, notably in the Jinding samples, contributed to values of a few tens to hundreds of ppm in a limited number of spots.

Nickel concentrations are <1 ppm in almost all analytical spots; outliers of up to a few tens of ppm are readily attributed to inclusions of Fe-(Ni)-minerals.

Measured *lead* concentrations vary over several orders of magnitude. The majority of the higher concentrations (e.g., in Jinding, or in the massive sulphide deposits) can be readily attributed to inclusions of galena and other Pb-bearing minerals. In the samples from the MVT deposits, particularly Mengxing, however, consistent concentrations and flat time-resolved depth profiles (Fig. 15g) point to incorporation of Pb in solid solution up to several hundred ppm (e.g., sample M-11, mean 386 ± 84 ppm).

Only three samples contrast with the otherwise low (<3–5 ppm) concentrations of *antimony*: samples 1086 (Huize; Fig. 15e), M1 (Mengxing) and 155–26 (Jinding), with concentrations up to ~300 ppm and means of 64, 88 and 46 ppm, respectively. In all three samples, Sb concentrations are mostly attributable to inclusions and tend to correlate with higher Cu content. There are, however, several individual spots, notably in sample M1, that give flat depth profiles corresponding to concentrations of several tens of ppm Sb, again correlating with Cu concentration.

Selenium concentrations in sphalerite are, at best, a couple of ppm in all samples, except those from the two skarns. In the low-Fe sample from Hetaoping (HTP163), concentrations average 57 ppm, whereas the two higher-Fe samples have somewhat lower concentrations (mean 19 ppm). A contrasting trend is seen in Luziyuan, where each sample shows a narrow, but different range of Se concentrations. The sample poorest in Fe (LZY47) contains 95–137 ppm Se while sample LZY61 contains 12–21 ppm: the highest-Fe sample (LZY29) contains very little Se (<4 ppm).

Tin concentrations in sphalerite from all deposits are <2 ppm, except for Laochang and Dabaoshan where consistent concentrations of 3–38 and 2–47 ppm, respectively, are noted, and Bainiuchang. In the latter, the two samples display variation over three orders of magnitude from a <10 ppm to >2500 ppm. There is no direct correlation between high-Sn values and regular or irregular time-resolved depth profiles, indicating that both lattice-bound and Sn-mineral inclusions Sn are present in sphalerite with high-Sn values, i.e., as high as thousands ppm (3BNC; Fig. 16a–c). The inclusions are most likely to be stannite given the fact that irregular Sn profiles are mirrored by Cu (and to some extent also Ag). In the second sample from Bainiuchang (10BNC), there is a correlation

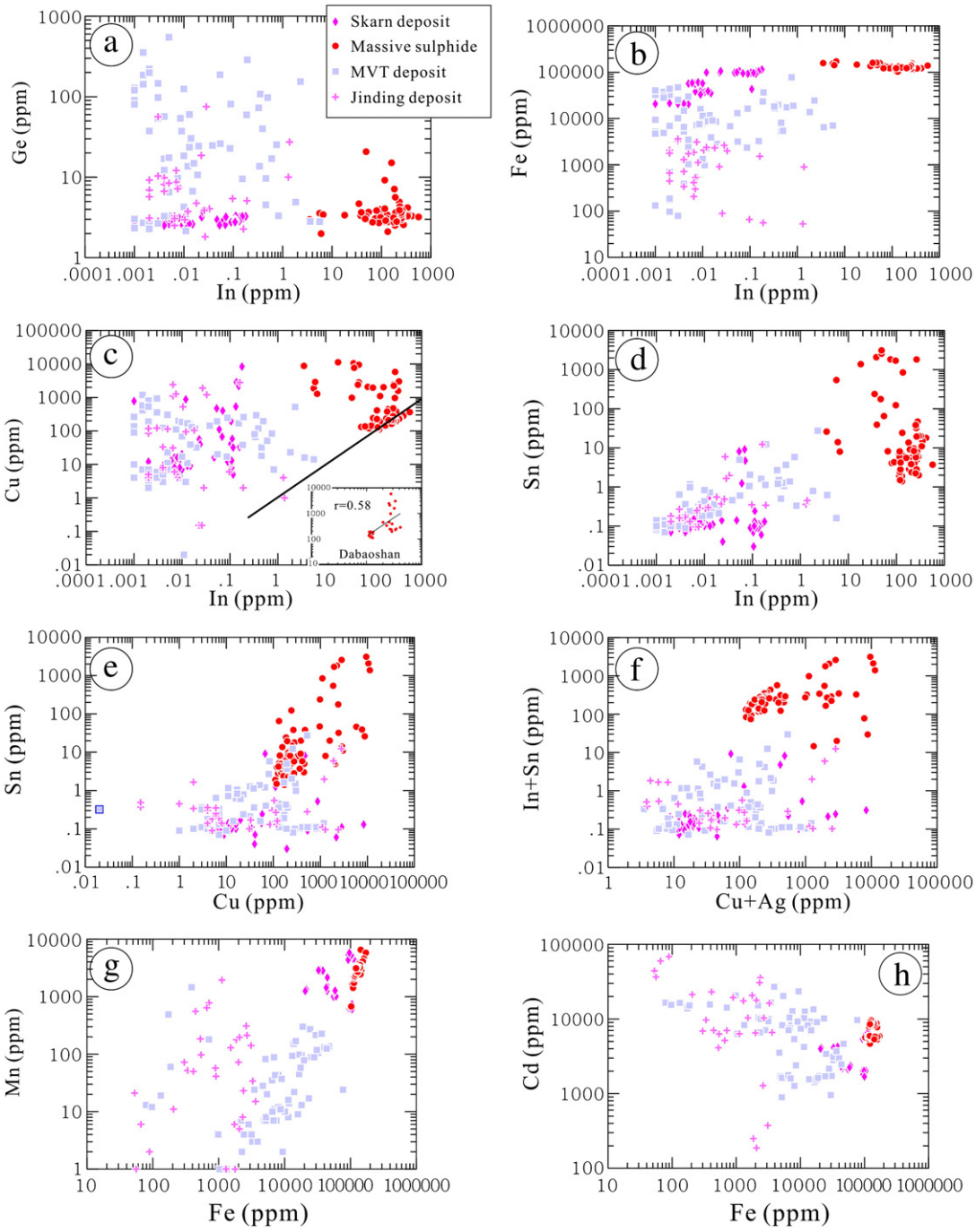

Fig. 17. Binary plots of (a) In vs. Ge, (b) In vs. Fe, (c) In vs. Cu, (d) In vs. Sn, (e) Cu vs. Sn, (f) (Cu + Ag) vs. (In + Sn), (g) Fe vs. Mn and (h) Fe vs. Cd, in sphalerite from Pb–Zn deposits in South China. Inset on (c) illustrates the relationship between In and Cu in Dabaoshan sphalerite only.

between Sn content and density of chalcopyrite exsolutions in sphalerite (Fig. 16d–f).

Tellurium concentrations are exceptionally low (generally < minimum detection limit). Single spots of ~1 ppm are seen in each of Mengxing and Jinding.

Thallium concentrations are typically <1 ppm in sphalerite from Hetaoping and Luziyuan, Bainiuchang, Laochang, Dabaoshan and Huize. In Niujiaotang, black sphalerite is Tl-enriched (mean 12.3 ppm) compared to yellow sphalerite (mean 0.6 ppm). Mengxing sphalerite displays modest Tl enrichment (mean 8.7 ppm). Jinding stands out from the other deposits with respect to Tl concentration in sphalerite, with many spots having >10 ppm (Fig. 15h). The population shows a normal distribution centred on the mean of 15 ppm. The time-resolved depth profiles show, however, that, in about half the spots, Tl concentrations relate to microscopic inclusions, even if other profiles are flat.

Gold concentrations are generally around or below the minimum detection limit (~0.004 ppm). Six spots from Luziyuan gave concentrations between 0.1 and 0.5 ppm.

Uranium concentrations were much less than 1 ppm in all analysed sphalerite.

6.1. Data trends

Some elements are clearly enriched in only some sub-populations which stand out from others. The pronounced enrichment of In seen

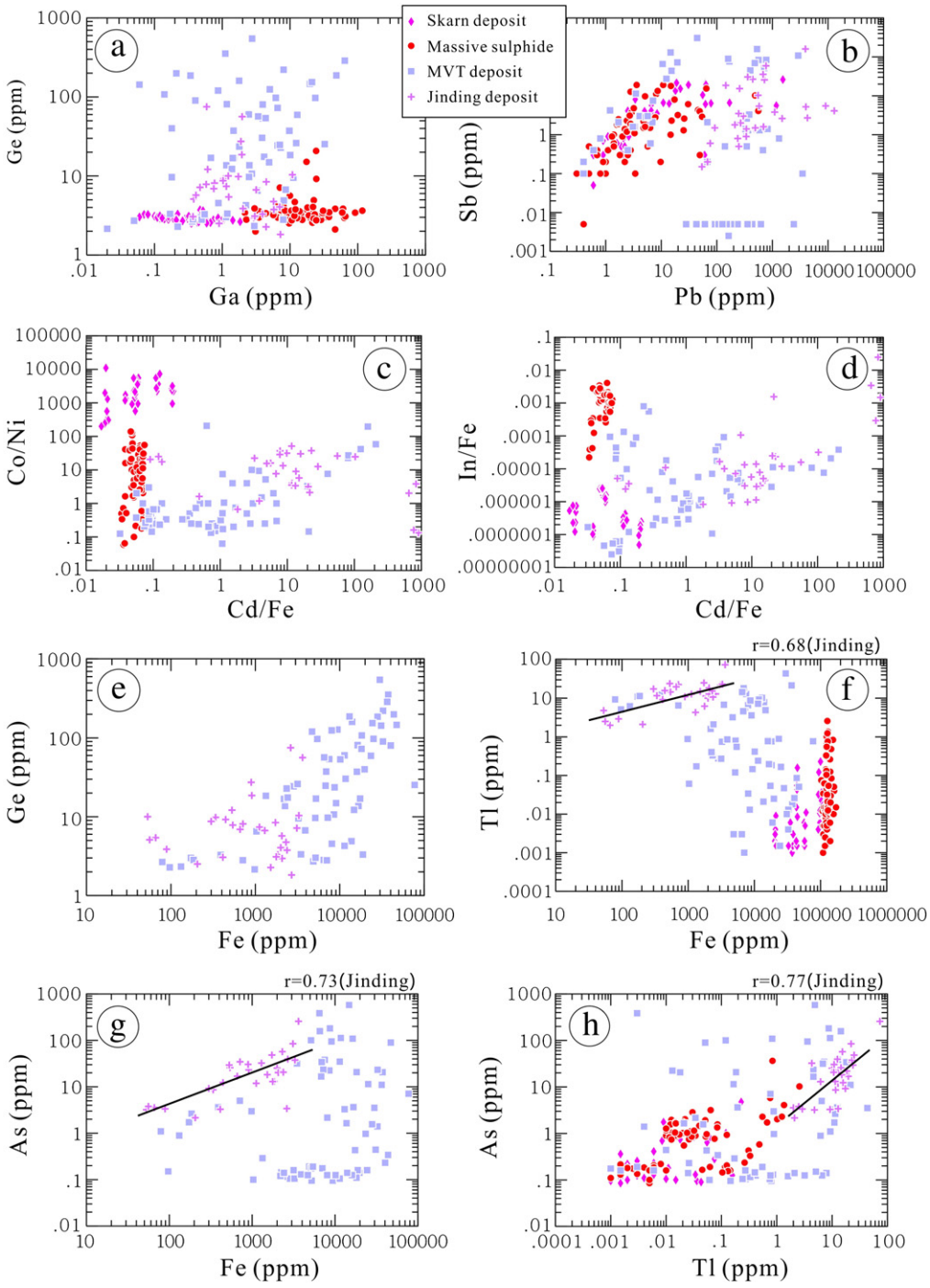

Fig. 18. Binary plots of (a) Ga vs. Ge, (b) Pb vs. Sb, (c) Co/Ni vs. Cd/Fe, (d) In/Fe vs. Cd/Fe, (e) Fe vs. Ge, (f) Fe vs. Tl, (g) Fe vs. As, and (h) Tl vs. As in sphalerite from Pb–Zn deposits in South China.

in sphalerite from the massive sulphide deposits and of Ge in sphalerite from the MVT deposits are two such examples. Binary plots are thus useful to discriminate the data. On a plot of In vs. Ge (Fig. 17a), the trend between these two elements is clearly seen. Indium is typically enriched in sphalerite from more proximal or hotter-fluid deposits, whereas Ge typifies lower-temperature systems. The distal character of the skarns sampled in this survey is amplified by their low In concentrations. Both the In vs. Fe and In (Fig. 17b) vs. Mn plots suggest evidence for positive correlation. However, this is probably a function of the Fe–Mn-rich character of sphalerite in the massive sulphides rather than any real trend.

There is a pronounced correlation between Cu and In (Fig. 17c), as would be expected given the accepted mechanism of In incorporation in sphalerite ($2Zn^{2+} \leftrightarrow Cu^{+} + In^{3+}$). The correlation is, however, far from perfect because of the presence of chalcopyrite disease in some samples, giving anomalously high Cu beyond that involved in the coupled substitution. In fact, most analytical spots lie on the Cu-rich side of the 1:1 Cu:In line. We illustrate this for the Dabaoshan sub-population (Fig. 17c, inset), in which more than half the individual spots lie on, or close to the 1:1 Cu:In line, but a minority (with chalcopyrite disease) do not. A further complicating factor is the likelihood of a competing substitution by which other elements with $^{3+}$ or $^{4+}$ oxidation states, such

as Sn, enter sphalerite. The good correlation between Sn and Cu (Fig. 17d) suggests that substitution mechanisms such as $3Zn^{2+} \leftrightarrow 2Cu^{+} + Sn^{4+}$ may operate independently of any $Cu^{+} + In^{3+}$ incorporation (e.g., in Bainiuchang). There is a marked correlation between Cu and Sn (Fig. 17e), even at lower concentrations. Enhanced concentrations of Sn in sphalerite, like In, can be indicative of either granitic or anomalously hot fluids. Incorporation of both Sn and In can also be facilitated by involvement of Ag+, such that a good correlation between (In + Sn) and (Cu + Ag) would also be expected. The binary plot for these variables (Fig. 17f) does indicate a positive correlation, but again, recognition of any clear pattern is impeded by chalcopyrite disease in part of the data suite.

A broad positive correlation is observed between Fe and Mn across the dataset (Fig. 17g), as well as within sub-populations for individual deposits. The Cd content, however, tends to decrease with increasing Fe content (Fig. 17h), although some sub-populations, notably Niujiaotang and Jinding, show erratic correlations. The latter are compounded by the presence of discrete types of sphalerite that are discriminated by Fe- but not by Cd-content. On the Ga vs. Ge plot (Fig. 18a), each deposit type defines a distinct field, yet there is no marked correlation between the two elements. Nickel and Co generally show similar geochemistry and often correlate with one another in any given dataset. A broad correlation is seen between the two elements in our sphalerite, even if Ni contents are generally very low and even the very high Co content of the skarns is not mirrored by enrichment in Ni (most <1 ppm).

We have noted above that our LA-ICPMS data for Sb and Pb in sphalerite indicate a likely combination of lattice-bound Sb and Pb, and the presence of sub-microscopic inclusions of minerals (such as sulphosalts) that contain these elements. The Sb–Pb binary plot (Fig. 18b) confirms such an interpretation, with individual sub-populations, e.g., Huize, showing strong positive correlations (r = 0.75). In the case of Huize, the time-resolved depth profiles corroborate the presence of inclusions of Pb-, Sb- and Cu-bearing mineral inclusions.

We have used the Cd/Fe ratio to obtain a better discrimination of the deposit types, given the characteristically low Cd/Fe ratio in the massive sulphide and skarn sphalerite. The Cd/Fe ratio, when plotted against Co/Ni or In/Fe (Fig. 18c,d) shows the complete dataset can be divided into two clear trends: one group with low (<0.1) Cd/Fe and variable Co/Ni or In/Fe, and a second group in which both Co/Ni and In/Fe show a systematic increase with Cd/Fe from ~0.1 up to >100.

If skarn and massive sulphide sphalerite data are excluded, Ge shows a strong positive correlation with Fe content (Fig. 18e), as does Ga, suggesting that Fe-rich sphalerite carries higher levels of both elements. Gallium exhibits both Ga^{2+} and Ga^{3+} oxidation states and thus may be expected to mimic iron in terms of substitution in sulphides. It is generally accepted that Fe enters sphalerite via a direct $Zn^{2+} \leftrightarrow Fe^{2+}$ substitution and that Fe^{3+} is not normally involved. Germanium, on the other hand, usually forms Ge^{4+} or Ge^{2+} ions, with Ge^{4+} being the more common oxidation state. Traditionally, substitution mechanisms for Ge in sphalerite have involved Ge^{4+} (e.g., Johan, 1988), but Cook et al. (2009) found no evidence for any coupled substitution involving Ge and proposed a direct $Zn^{2+} \leftrightarrow Ge^{2+}$ substitution. A conspicuous opposing trend is seen for Tl, in which the Fe-poorest sphalerites (mostly from Jinding) are highest in that element (Fig. 18f). On the corresponding plots of As vs. Fe (Fig. 18g) and As vs. Tl (Fig. 18h), there is a strong positive correlation between the two elements in the Jinding sub-set. Given that As- and Tl-bearing mineral inclusions were recognised in many of the time-resolved depth profiles, we believe that submicroscopic inclusions of fangite (Tl_3AsS_4) or a similar phase could be present.

7. Discussion

Our dataset is compiled on a suite of samples from different metallogenetic provinces, albeit within a restricted geographic area. Despite this, various trends relating to trace element distribution among deposits of different genetic type can be readily seen, and which can be compared to published data. In particular, notably because of the comparable range of elements and analytical work under the same conditions and in the same laboratory, the dataset complements the conspectus of compositional variation in sphalerite given by Cook et al. (2009).

In that study, the skarn deposits studied were more proximal, higher-temperature systems, characterised by elevated In, Cu and Sn. The skarns studied here do not show In enrichment, in line with their distal character. In common with the skarns analysed here, however, concentrations of Mn and, especially, Co were also high in the skarns investigated by Cook et al. (2009). We believe that a marked Co enrichment may typify skarn sphalerite, but cannot as yet substantiate a mechanism for this. Also consistent with pre-existing data are the insignificant Ag, Ga and Ge contents in Chinese skarn sphalerite and the modest enrichment in Se (a few tens of ppm).

Sphalerite from the massive sulphides in our dataset (two SEDEX deposits, Dabaoshan and Bainiuchang, and one VMS-style deposit, Laochang) shows strong enrichment in In and Sn. This enrichment in granitophile elements could be taken to support the argument for metal input during emplacement of younger granites. If this would, however, be the case, multiple generations of sphalerite would be expected and we would not see the observed variation between adjacent laser spots (e.g., in Bainiuchang; Fig. 16). Although many SEDEX/VMS deposits are indeed not especially rich in these elements, there are numerous notable SEDEX/VMS deposits in which sphalerite is strongly enriched in these elements (e.g., Neves Corvo, Kidd Creek, Sullivan, Brunswick no. 12; Briskey, 2005; Schwarz-Schampera and Herzig, 2002) and which contribute a large part of current world production of In, and also produce by-product Sn. The high-Sn values seen as inclusions of stannite from Bainiuchang could be associated with the granite overprint, given the fact the samples are from an orebody situated nearby younger (Yanshanian) intrusions intersected in drillcores some 200–300 m below. The high-Sn values where lattice-bound Sn can be inferred from the flat profiles are, however, most likely a characteristic of the syngenetic sphalerite. Likewise, the In enrichment in Zn-ores at Dabaoshan and Laochang is probably related to the specifics of the local metal source (more magmatic component) and proximity to source rather than overprinting of the primary massive sulphide by Cu–In–(Sn)-rich fluids during later magmatic events. In both cases, the remarkable consistency of measured In concentrations, steady Fe concentratons, ore textures and general ore morphology is more typical of syngenetic sphalerite. Despite the fact that the three deposits are hosted within strata of different ages and in different metallogenic units hundreds of km apart, they are conspicuous by their content of these elements.

Enrichment in Ge in MVT deposits is well-known and these deposits, and comparable carbonate-replacement, and sandstone- or shale-hosted deposits, are the main source of Ge. It is therefore not surprising that sphalerite from the MVT deposits in this study (e.g., Huize) are richer in this element. The high (but variable) Ge concentrations in Huize sphalerite are nonetheless lower than those in galena from the same deposit (mean 1300 ppm; Zhang, 2003), lending weight to a marked partitioning of Ge between the two minerals when both are present. Germanium concentrations in sphalerite will be higher where galena is negligible or absent (e.g., samples from Tres Marias, Mexico, analysed by Cook et al., 2009).

Both Cd and Tl are also typically higher in lower-temperature deposits hosted within sedimentary sequences and deposits of this type (e.g., Red Dog, Alaska; Kelley et al., 2004) produce a large part of current world production. Enrichment of Cd and other elements in the MVT deposits (including Jinding) is source-specific. At Niujiaotang, the Cd-enrichment has been attributed to an initial, possibly biogenic mineralization. Similar models might also be associated with

enrichment in Tl and As in Jinding. From the perspective of sphalerite geochemistry, Jinding shares the features of the MVT deposits, as would be expected by the involvement of comparable basinal fluids. What makes Jinding stand out from the MVT deposits is high abundance of barite inclusions in sphalerite (Fig. 12l) which are consistent with the higher salinity basinal fluids.

A feature of the MVT deposits is the presence of distinct generations of sphalerite characterised by differences in Fe content. There does not, however, appear to be any significant correlation between Cd content and sphalerite colour in the studied deposits. Late, low-temperature crystallisation of greenockite along fractures, or replacement on the margins of sphalerite, may have influenced Cd distribution in sphalerite from Niujiaotang to a limited extent. These relationships (Fig. 12j) demand further work by transmission electron microscopy on foils prepared by focussed ion beam methods across the replacement boundary. This would test the identity of the phases, and whether they are the products of exsolution or feature disordered lattice-scale intergrowths. The material is interesting for understanding the underlying crystal chemistry of the system CdS–ZnS, by analogy to the system ZnS–$CuInS_2$ (Schorr and Wagner, 2005), in which lamellar exsolution of phases with sphalerite-, wurtzite and chalcopyrite-type structures are observed.

All the sphalerite-bearing samples investigated show evidence of complex textural reworking. Despite this, sphalerite is a refractory mineral and we see negligible evidence for recrystallisation or wholesale modification of sphalerite compositions by later events. Our data thus show the usefulness of trace element distributions in sphalerite as a tracer of genetic type. Systematic analysis of a larger sample set covering all orebodies, especially from the 3 massive sulphides, could be used to test ideas about metal source and proximity to source. Tin and indium would seem to have particular application in identifying syngenetic origin vs. overprinting.

8. Conclusions

1. The geochemistry of sphalerite from 9 deposits of different age and metallogenic province in South China can be used to assign them into genetic types (skarn, syngenetic massive sulphide, MVT-type), even when their origin is debated based on other criteria.
2. Sphalerite from each genetic class of deposit shows a distinct chemical signature. The skarns feature high Co and Mn; their distal character is reflected by low In. The syngenetic massive sulphides have In, Sn and Ga and the MVT-type are enriched in Ge, Cd, Tl and As.
3. Given the refractory character of sphalerite, trace element analysis of sphalerite shows promise as a tracer of overprinting, which may assist in defining the geochemical signature of different metallogenic epochs in a region as geologically complex as South China.
4. The time-resolved depth profiles for sphalerite from the Chinese deposits document solid solution for a number of trace elements whose ability to enter the crystal structure of sphalerite has been previously debated (Ag, Sn, Tl, Sb).

Acknowledgements

This research project was jointly supported by the National '973 Project' (No. 2009CB421003), the Knowledge Innovation Program of the Chinese Academy of Sciences (Grant No: KZCX2-YW-136-2, KZCX2-YW-111-03), and the Foundation of State Key Laboratory of Ore Deposit Geochemistry. The senior author wishes to thank the China Science Foundation for funding his sabbatical visit to the University of Adelaide during which time this research was carried out. We are greatly indebted to Chief Engineer Zhou Yunman (Yunnan Geology and Mineral Resources Ltd.), Chief Engineer Chen Guoyong (No.104 Geological Team of Guizhou Bureau of Geology and Minerals) and Chief Engineer Liu Cong (Dabaoshan Mining Limited Company, Guangdong Province) who assisted with sampling. We gratefully thank the Ore Geology Reviews reviewers Gu Lianxing and Liu Junlai for their valuable comments, and Associate Editor Franco Pirajno for his suggestions for improvement of the manuscript. This is contribution no. 139 of the Centre for Tectonics, Resources and Exploration (TRaX).

Appendix A. Supplementary data

Supplementary data to this article can be found online at doi:10.1016/j.oregeorev.2011.03.001.

References

Beaudoin, G., 2000. Acicular sphalerite enriched in Ag, Sb, and Cu embedded within colour banded sphalerite from the Kokanee Range, BC. Canadian Mineralogist 38, 1387–1398.
Briskey, J.A., 2005. Indium in zinc-lead and other mineral deposits — a reconnaissance Survey of 1118 Indium Analyses published before 1985. U.S. Geological Survey Open-File Report 2005–1209, 8 pp. + tables.
Bureau of Geology and Mining of Yunnan Province, 2006. The report about major exploring problem in southern section of 'Sanjiang' region. Unpublished report, unpaginated. (in Chinese).
Cai, J.H., Liu, J.Q., 1993. Research and its application on the inclusions characteristics in the Dabaoshan polymetallic deposit, Northern Guangdong. Journal of Mineral Petrology 13 (1), 33–40 (in Chinese with English abstract).
Chen, B.Y., Wang, Z.R., Peng, S.L., Zhang, Y.X., Chen, W., 2000a. A discussion about the genesis of Laochang polymetallic deposit, Yunnan. Yunnan Geology 21 (2), 134–144 (in Chinese with English abstract).
Chen, B.Y., Wang, Z.R., Zhang, Y.X., Chen, W., 2000b. Metallogenic conditions and prospecting criteria of Laochang lateritic silver deposit, Lancang. Journal of Central South University of Technology 31 (3), 195–198 (in Chinese with English abstract).
Chen, G.Y., Zhong, Y.T., Huang, G.S., 1992. Geological characters and conditions of mineralization of Niujiaotang zinc deposit, Duyun. Guizhou Geology 9 (3), 203–211 (in Chinese).
Chen, J.F., Jahn, B.M., 1998. Crustal evolution of southeastern China: Nd and Sr isotopic evidence. Tectonophysics 284, 101–133.
Chen, X.M., Deng, J., Bai, J.G., Shen, C.H., 2000. Mineralization fluid system of Palaeozoic sedimentary basin at Bainiuchang, Yunnan Province. GeoScience 14 (2), 175–178 (in Chinese with English abstract).
Chen, Y.C., Chang, Y.F., Pei, R.F., Ren, J.S., Tang, Z.L., Zhai, Y.S., 2007. Chinese Mineralization System and Assessment of Regional Mineralization. Geological Publishing House, Beijing. 962 pp. (in Chinese).
Chen, Y.Q., Lu, Y.X., Xia, Q.L., Jiang, C.X., Liu, H.G., Lu, Z.C., 2005. Geochemical characteristics of the Hetaoping Pb–Zn deposit, Baoshan, Yunnan, and its genetic model and ore prospecting model pattern. Geology in China 32 (1), 90–99 (in Chinese with English abstract).
Ciobanu, C.L., Cook, N.J., 2004. Skarn textures: a case study of the Ocna de Fier-Dognecea orefield, Banat, Romania. Ore Geology Reviews 24, 315–370.
Cook, N.J., 1996. Mineralogy of the sulphide deposits at Sulitjelma, northern Norway. Ore Geology Reviews 11, 303–308.
Cook, N.J., Spry, P.G., Vokes, F.M., 1998. Mineralogy, paragenesis and metamorphism of ores in the Bleikvassli Pb–Zn–(Cu) deposit, Nordland, Norway. Mineralium Deposita 34, 35–56.
Cook, N.J., Ciobanu, C.L., Pring, A., Skinner, W., Danyushevsky, L., Shimizu, M., Saini-Eidukat, B., Melcher, F., 2009. Trace and minor elements in sphalerite: a LA-ICP-MS study. Geochimica et Cosmochimica Acta 73, 4761–4791.
Danyushevsky, L.V., Robinson, P., Gilbert, S., Norman, M., Large, R., McGoldrick, P., Shelley, J.M.G., 2011. Routine quantitative multi-element analysis of sulphide minerals by laser ablation ICP-MS: standard development and consideration of matrix effects. Geochemistry: Exploration, Environment, Analysis 11, 51–60.
Deng, B.F., 1995. Metallogenic model of mercury and lead-zinc deposits in Baoshan-Zhenkang area. Yunnan Geology 14 (4), 355–364 (in Chinese).
Deng, J., Yang, L.Q., Sun, Z.S., Wang, J.P., Wang, Q.F., Cheng, X.M., Zhou, Y.H., 2005. Late-paleozoic fluid systems and their ore-forming effects in the Yuebei Basin, China. Acta Geological Sinica (English Edition) 79 (5), 673–687.
Di Benedetto, F., Bernardini, G.P., Costagliola, P., Plant, D., Vaughan, D.J., 2005. Compositional zoning in sphalerite crystals. American Mineralogist 90, 1384–1392.
Dong, S.W., Zhang, Y.Q., Long, C.X., Yang, Z.Y., Ji, Q., Wang, T., Hu, J.M., Chen, X.H., 2007. Jurassic tectonic revolution in China and new interpretation of the Yanshan movent. Acta Geologica Sinica 81, 1449–1460 (in Chinese with English abstract).
Dong, W.W., Chen, S.L., 2007. The characteristics and genesis of Luziyuan Pb–Zn deposit, Zhengkang. Yunnan Geology 26 (4), 404–410 (in Chinese with English abstract).
Fleischer, M., 1955. Minor elements in some sulfide minerals. Economic Geology 50th Anniversary volume, part II, pp. 970–1024.
Gu, L.X., Zaw, K., Hu, W.X., Zhang, K.J., Ni, P., He, J.X., Xu, Y.T., Lu, J.J., Lin, C.M., 2007. Distinctive features of Late Palaeozoic massive sulphide deposits in South China. Ore Geology Reviews 31, 107–138.
Han, R.S., Liu, C.Q., Huang, Z.L., Chen, J., Ma, D.Y., Lei, L., Ma, G.S., 2007. Geological features and origin of the Huize carbonate-hosted Zn–Pb–(Ag) District, Yunnan, South China. Ore Geology Reviews 31, 360–383.

Hou, Z.Q., Li, H.Y., 1998. A tentative discussion on the mantle plume tectonics and metallogenic system as exemplified by the Sanjiang Tethyan metallogenic domain. Mineral Deposits 17 (2), 97–113 (in Chinese with English abstract).
Hou, Z.Q., Zaw, K., Pan, G.T., Mo, X.X., Xu, Q., Hu, Y.Z., Li, X.Z., 2007. Sanjiang Tethyan metallogenesis in S.W. China: tectonic setting, metallogenic epochs and deposit types. Ore Geology Reviews 31, 48–87.
Hua, R.M., Chen, P.R., Zhang, W.L., Lu, J.J., 2005. Three large-scale metallogenic events related to the Yanshanian Period in Southern China. In: Mao, J.W., Bierlein, F.P. (Eds.), Mineral Deposit Research: Meeting the Global Challenge Proceedings of the 8th Biennial SGA Meeting Beijing, China. Springer, pp. 401–404.
Huang, Z.L., Li, W.B., Chen, J., Han, R.S., Liu, C.Q., Xu, C., Guan, T., 2003. Carbon and oxygen isotope constraint on mantle fluid involvement in the mineralization of Huize super-large Pb–Zn deposits, Yunnan Province, China. Journal of Geochemical Exploration 78–79, 637–642.
Huston, D.L., Sie, S.H., Suter, G.F., Cooke, D.R., Both, R.A., 1995. Trace elements in sulfide minerals from eastern Australian volcanic-hosted massive sulfide deposits; Part I, Proton microprobe analyses of pyrite, chalcopyrite, and sphalerite, and Part II, Selenium levels in pyrite; comparison with $\delta^{34}S$ values and implications for the source of sulfur in volcanogenic hydrothermal systems. Economic Geology 90, 1167–1196.
Ishihara, S., Endo, Y., 2007. Indium and other trace elements in volcanogenic massive sulphide ores from the Kuroko, Besshi and other types in Japan. Bulletin, Geological Survey of Japan 58, 7–22.
Ishihara, S., Hoshino, K., Murakami, H., Endo, Y., 2006. Resource evaluation and some genetic aspects of indium in the Japanese ore deposits. Resource Geology 56, 347–364.
Jin, X.C., Wang, Y.Z., Xie, G.L., 2003. Devonian to Triassic successions of the Changning–Menglian Belt, Western Yunnan, China. Acta Geologica Sinca 77, 440–456.
Johan, Z., 1988. Indium and germanium in the structure of sphalerite: an example of coupled substitution with copper. Mineralogy and Petrology 39, 211–229.
Kang, Y.T., 1982. Structures and metallogenesis at depths east of Honghe, Yunnan. Yunnan Geology 1 (1), 17–28 (in Chinese).
Kelley, K.D., Leach, D.L., Johnson, C.A., Clark, J.L., Fayek, M., Slack, J.F., Anderson, V.M., Ayuso, R.A., Ridley, W.I., 2004. Textural, compositional, and sulfur isotope variations of sulfide minerals in the Red Dog Zn–Pb–Ag deposits, Brooks Range, Alaska: implications for ore formation. Economic Geology 99, 1509–1532.
Li, F., Chen, H., Lu, W.J., Luo, S.L., 2010. Rock-forming ages of the Laochang granite-porphyry, Lancang, Yunnan and their geological significance. Geotectonia et Metallogenia 34 (1), 84–91 (in Chinese with English abstract).
Li, H.J., Tian, X., 1995. The study on fluid inclusion and its ore-forming physicochemical conditions for Langcang Pb–Zn–Ag–Cu deposit. Mineral Resources and Geology 9 (2), 107–111 (in Chinese).
Li, L., Duan, J.R., Li, F., Ma, Y., Huang, D.Y., 1996. Geologic features and multiperiodic syntopogenic metallogenesis of the Laochang Cu-polymetal deposit in Lancang, Yunnan. Yunnan Geology 15 (3), 246–256 (in Chinese with English abstract).
Li, W.B., Huang, Z.L., Wang, Y.X., Chen, J., Han, R.S., Xu, C., Guan, T., Yin, M.D., 2004. Age of the giant Huize Zn–Pb deposits determined by Sm–Nd dating of hydrothermal calcite. Geological Review 50 (3), 189–195 (in Chinese with English abstract).
Li, W.H., Li, L., Zhao, R.K., Chen, Y., Zhao, C.S., Zeng, G.R., Yang, C.L., 1985. On the sedimentary ore-forming factors of the Pb–Zn deposit at Mengxing, Longling County. Yunnan Geology 4 (8), 234–244 (in Chinese with English abstract).
Li, X.H., 1997. Timing of the Cathaysia Block formation: constraints from SHRIMP U–Pb zircon geochronology. Episodes 20, 188–192.
Li, X.M., Tan, K.X., Gong, W.J., Gong, G.L., 2000. Study on the metallogenic epoch of the Jinding lead-zinc deposit with apatite fission track analysis. Getectonica et Metallogenia 24 (3), 282–286 (in Chinese with English abstract).
Li, Z.Q., Chen, Y.G., Zhang, T.S., Ren, Z.J., Zhao, C.S., Li, W.Z., 2005. Geological characters and sustainable mineral resources of Mengnuo Pb–Zn ore deposit in Yunnan. Contributions to Geology and Mineral Resources Research 20 (2), 123–126 131. (in Chinese with English abstract).
Li, Z.X., Li, X.H., Zhou, H.W., Kinny, P.D., 2002. Grenvillian continental collision in south China: new SHRIMP U–Pb zircon results and implications for the configuration of Rodinia. Geology 30, 163–166.
Liang, H.Y., Campbell, I.H., Allen, C.M., Sun, W.D., Yu, H.X., Xie, Y.W., Zhang, Y.Q., 2007. The age of the potassic alkaline igneous rocks along the Ailao Shan-Red River Shear Zone: implications for the onset age of left-lateral shearing. Journal of Geology 115, 231–242.
Liu, J.L., Wang, A.J., Cao, D.H., Xiu, Q.Y., 2004. Structure and evolution of the post-collisional fault structures in the Three River Orogenic Belt, exemplified by the Cenozoic Jianchuan–Lanping Basin. Geological Journal of China Universities 10, 488–499 (in Chinese with English abstract).
Liu, J.L., Song, Z.J., Cao, S.Y., Zhai, Y.F., Wang, A.J., Gao, L., Xiu, Q.Y., Cao, D.H., 2006. The dynamic setting and processes of tectonic and magmatic evolution of the oblique collision zone between Indian and Eurasian plates: exemplified by the tectonic evolution of the Three River region, eastern Tibet. Acta Petrologica Sinica 22, 775–786 (in Chinese with English abstract).
Liu, J.L., Cao, S.Y., Zhai, Y.F., Song, Z.J., Wang, A.J., Xiu, Q.Y., Cao, D.H., Gao, L., Guan, Y., 2007a. Rotation of crustal blocks as an explanation of Oligo-Miocene extension in Southeastern Tibet — evidenced by the Diancangshan and nearby metamorphic core complexes. Earth Science Frontiers 14, 40–48 (in Chinese with English abstract).
Liu, J.L., Wang, A.J., Xia, H.R., Zhai, Y.F., Gao, L., Xiu, Q.Y., Zhang, Z.C., Zhao, Z.D., Cao, D.H., 2010. Cracking mechanisms during galena mineralization in a sandstone-hosted lead-zinc ore deposit: case study of the Jinding giant sulphide deposit, Yunnan, SW China. Mineralium Deposita 45, 567–582.
Liu, J.S., Zhang, H.P., Ouyang, Y.F., Zhang, C.H., 2007b. Bainiuchang super-large silver-polymetallic ore deposit related to granitic magmatism in Mengzi, Yunnan. Journal of Central South University of Technology 14 (4), 568–574.
Liu, Z.-Q., Li, X.-Z., Ye, Q.-T., Luo, J.-N., Shen, G.-F., 1993. Division of Tectono-Magmatic Zones and the Distribution of Deposits in the Sanjiang Area. Geological Publishing House, Beijing. 246 pp. (in Chinese with English abstract).
Long, H.S., 2009.Geochronology and Geochemistry of the Laochang Large Silver Polymetallic Deposit, Yunnan Province, China. Unpublished Ph.D Thesis, Institute of Geochemistry, Chinese Academic of Science, Guiyang, 188 pp. (in Chinese with English abstract).
Luo, N.H., 1985. The geological and geochemical features and the origin of Dabaoshan polymetallic deposit in Guangdong Province. Journal of Guilin College of Geology 5 (2), 183–195 (in Chinese with English abstract).
Metcalfe, I., 2006. Palaeozoic and Mesozoic tectonic evolution and palaeogeography of East Asian crustal fragments: the Korean Peninsula in context. Gondwana Research 9, 24–46.
Mo, X.X., Deng, J.F., Lu, F.X., 1994. Volcanism and the evolution of Tethy in Sanjiang area, southwestern China. Journal of Southeast Asian Earth Science 9, 325–333.
Oftedahl, I., 1940. Untersuchungen über die Nebenbestandteile von Erzmineralien norwegischer zinkblendführender Vorkommen. Skrift. Norsk Videnskabs Akademi Oslo, Mathematik-Naturvidenskab Kl 8, 1–103.
Pan, G.-T., Chen, Z.-L., Li, X.-Z., 1997. Tectonic Evolution of the East Tethys Geology. Geological Publishing House, Beijing. 257 pp. (in Chinese with English abstract).
Pan, G.T., Xiao, Q.H., Lu, S.N., Deng, J.F., Feng, Y.M., Zhang, K.X., Zhang, Z.Y., Wang, F.G., Xing, G.F., Hao, G.J., Feng, Y.F., 2009. Subdivision of tectonic units in China. Geology in China 36 (1), 1–28 (in Chinese with English abstract).
Qiu, Y., Gao, S., McNaughton, N.J., Groves, D.I., Ling, W., 2000. First evidence of >3.2 Ga continental crust in the Yangtze craton of south China and its implications for Archean crustal evolution and Phanerozoic tectonics. Geology 28, 11–14.
Schorr, S., Wagner, G., 2005. Structure and phase relations of the $Zn_{2x}(CuIn)_{1-x}S_2$ solid solution series. Journal of Alloys and Compounds 396, 202–207.
Schwarz-Schampera, U., Herzig, P.M., 2002. Indium: Geology, Mineralogy, and Economics. Springer. 257 pp.
Shen, W.Z., 2006. Comment on the isotopic age data of basement metamorphic rocks in Cathaysia Block. Geological Journal of China Universities 12, 475–482 (in Chinese with English abstract).
Song, S.M., Hu, K., Jiang, S.Y., Li, K., 2007. The He–Ar–Pb–S isotope trace on ore-forming fluid in Dabaoshan Hill polymetallic deposit, North Guangdong. Contributions to Geology and Mineral Resources Research 22 (2), 87–92 99. (in Chinese with English abstract).
Tao, Y., Hu, R.Z., Zhu, F.L., Ma, Y.S., Ye, L., Cheng, Z.T., 2010. Ore-forming age and the geodynamic background of the Hetaoping lead-zinc deposit in Baoshan, Yunnan. Acta Petrologica Sinica 26 (6), 1760–1772 (in Chinese with English abstract).
Tu, G.Z., 1988. Geochemistry of Strata-bound Ore Deposits in China (Volumes III). Science Press, Beijing. 388 pp. (in Chinese with English abstract).
Wang, H.N., Zhou, L.Y., 2006. A futher understanding in geological structure of South China. Geological Journal of China Universities 12, 457–465 (in Chinese with English abstract).
Wang, H.Y., 1993. Geochemicial Characteristics of lead-zinc deposit in Guizhou. Geology of Guizhou 10 (4), 274–289 (in Chinese).
Wang, J.X., 2006. Geological characteristics and ore prospecting orientation of lead zinc polymetallic deposit in south Dabaoshan, Guangdong. Mineral Resources and Geology 20 (2), 142–146 (in Chinese with English abstract).
Wang, L., Hu, M.G., Yang, Z., Qi, W.J., Xia, J.L., Chen, K.X., (in press). U–Pb and Re–Os geochronology and geodynamic setting of the Dabaoshan polymetallic molybdenum deposit, northern Guangdong Province, South China. Ore Geology Reviews.
Xia, Q.L., Chen, Y.Q., Lu, Y.X., Jiang, C.X., Liu, H.G., L , Z.C., 2005. Geochemistry, fluid inclusion, and stable isotope studies of Luziyuan Pb–Zn deposit in Yunnan Province, Southwestern China. Earth Science-Journal of China University of Geosciences 30 (2), 177–186 (in Chinese with English abstract).
Xie, H.J., Zhu, C.H., Zhang, Q., Wang, D.P., Fan, L.W., 2009. Sulfur isotopic composition of the Bainiuchang super-large Ag polymetallic deposit, Yunnan Province, China: implications for the source of sulfur in ore-forming fluids. Chinese Journal of Geochemistry 28, 284–292.
Xu, X.S., O'Reilly, S.Y., Griffin, W.L., Wang, X.L., Pearson, N.J., He, Z.Y., 2007. The crust of Cathaysia: age, assembly and reworking of two terranes. Precambrian Research 158, 51–78.
Xu, W.X., Li, H., Chen, M.Y., Huang, D.X., Zhang, F.T., Wang, L.M., 2008. Isotope evidence of material sources of the Dabaoshan polymetallic deposit. Acta Geoscientica Sinica 29 (6), 684–690 (in Chinese with English abstract).
Xue, B.G., 1998. Mineralization characteristics of the Laochang Ag–Pb polymetallic deposit, Lanchang. Mineral Resources and Geology 12 (1), 26–32 (in Chinese with English abstract).
Xue, C.D., Han, R.S., Hu, Y.Z., Zou, H.J., Zhu, Y.Y., 2006. Physical chemistry study on the Ore-forming process of the hetaoping Pb–Zn-polymetallic deposit, baoshan county, yunnan province, China. Geochimica et Cosmochimica Acta 70, A715.
Xue, C.D., Han, R.S., Yang, H.L., Yang, Z.M., Tian, S.H., Liu, Y.Q., Hao, B.W., 2008. Isotope geochemical evidence for ore-forming fluid resources in Hetaoping Pb–Zn deposit, Baoshan , northwestern Yunnan. Mineral Deposits 27 (2), 243–252 (in Chinese with English abstract).
Xue, C.J., Chen, Y.C., Wang, D.H., Yang, J.M., Yang, W.G., Zeng, R., 2003. Geology and isotopic composition of helium, neon, xenon and metallogenic age of Jinding and Baiyangping ore deposits, northwest Yunnan, China. Science in China 46 (8), 789–800 (in Chinese).
Xue, C.J., Chi, G.X., Chen, Y.C., Zeng, R., Gao, Y.B., Qing, H.R., 2007a. The fluid dynamic process of large-scale mineralization in the Lanping Basin, Yunnan, SW China: evidence from fluid inclusions and basin fluid modeling. Earth Science Frontiers 14 (5), 147–157.
Xue, C.J., Zeng, R., Liu, S.W., Chi, G.X., Qing, H.R., Chen, Y.C., Yang, J.M., Wang, D.H., 2007b. Geologic, fluid inclusion and isotopic characteristics of the Jinding Zn–Pb

deposit, western Yunnan, South China: a review. Ore Geology Reviews 31, 337–359.
Yang, Z.Q., 1997. Origin of the Dabaoshan massive sulphide deposit: Devonian sea-floor thermal events. Geology and Mineral Resources of South China 14 (1), 7–17 (in Chinese with English abstract).
Ye, L., Liu, T.G., 1999. Sphalerite chemistry, Niujiaotang Cd-rich zinc deposit, Guizhou, Southwest China. Journal of Geochemistry 18 (1), 62–68.
Ye, L., Liu, T.G., Shao, S.X., 2000. Geochemistry of mineralizing fluid of Cd-rich zinc deposit: taking Niujiaotang Cd-rich zinc deposit, Duyun, Guizhou for example. Geochimica 29 (6), 597–603 (in Chinese with English abstract).
Ye, L., Pan, Z.P., Li, C.Y., Liu, T.G., Xia, B., 2005. Isotopic geochemical characters in Niujiaotang Cd rich zinc deposit, Duyun, Guizhou. Journal of Mineralogy and Petrology 25 (2), 70–74 (in Chinese with English abstract).
Ye, L., Gao, W., Cheng, Z.T., Yang, Y.L., Tao, Y., 2010. LA-ICPMS zircon U–Pb geochronology and petrology of the Muchang alkali granite, Zhenkang County, Western Yunnan Province, China. Acta Geologica Sinica (English edition) 84, 1488–1499.
Ye, L., Cook, N.J., Liu, T.G., Ciobanu, C.L., Gao, W., Yang, Y.L., (in press). The Niujiaotang Cd-rich zinc deposit, Duyun, Guizhou Province, Southwest China: ore genesis and mechanisms of cadmium concentration. Mineralium Deposita.
Yu, J.H., Wang, L.J., Wei, Z.Y., Sun, T., Shu, L.S., 2007. Phanerozoic metamorphic episodes and characteristics of Cathaysia Block. South China. Geological Journal of China Universities 13, 474–483 (in Chinese with English abstract).
Yu, J.H., Wang, L.J., O'Reilly, S.Y., Shu, L.S., Sun, T., 2009. Paleoproterozoic basement beneath the southern Jiangxi Province: evidence from U–Pb ages and Lu–Hf isotopes in zircons from the Doushui lamprophyre. Chinese Science Bulletin 54, 1555–1563.
Zaw, K., Peters, S.G., Cromie, P., Burrett, C., Hou, Z.Q., 2007. Nature, diversity of deposit types and metallogenic relations of South China. Ore Geology Reviews 31, 3–47.
Zhang, C.Q., Mao, J.W., Liu, F., Li, H.M., 2005a. K–Ar dating of altered clay minerals from Huize Pb–Zn deposit in Yunnan Province and its geological significance. Mineral Deposits 24 (3), 317–324 (in Chinese with English abstract).
Zhang, C.Q., Mao, J.W., Wu, S.P., Li, H.M., Liu, F., Guo, B.J., Gao, D.R., 2005b. Distribution, characteristics and genesis of Mississippi Valley-Type lead zinc deposit in Sichuan–Yunnan–Guizhou area. Mineral Deposits 24 (3), 336–348 (in Chinese with English abstract).
Zhang, J.J., Zhong, D.L., Sang, H.Q., Zhou, Y., 2006. Structural and geochronological evidence for multiple episodes of deformation since Paleocene along the Ailaoshan-Red River Shear Zone, southeastern Asia. Chinese Journal of Geology 41, 291–310 (in Chinese with English abstract).
Zhang, M., 2003. The enrichment mechanism and its geochemical feature of Ge and Cd in Huize Pb–Zn–Ge–Cd deposit. Unpublished Master Thesis, Chengdu University of Technology, Chengdu, 69 pp. (in Chinese with English Abstract).
Zhang, Q., 1987. Trace elements in galena and sphalerite and their geochemical significance in distinguishing the genetic types of Pb–Zn ore deposits. Chinese Journal of Geochemistry 6, 177–190.
Zhang, Z.L., Huang, Z.L., Rao, B., Li, W.B., Yan, Z.F., 2005. Study on the ore-forming fluid characteristics of Huize Pb–Zn ore deposit. Contributions to Geology and Mineral Resources Research 20 (2), 115–122 (in Chinese with English abstract).
Zhao, Z., 2007. The Jinding Pb–Zn deposit of Lanping—a lead facies sedex ore deposit. Yunnan Geology 26 (1), 1–14 (in Chinese with English abstract).
Zheng, J.P., Griffin, W.L., O'Reilly, S.Y., Zhang, M., Pearson, N.J., Pan, Y.M., 2006. Widespread Archean basement beneath the Yangtze craton. Geology 34, 417–420.
Zhou, C.X., Wei, S.S., Guo, J.Y., Li, C.Y., 2001. The source of metals in the Qilichang Zn–Pb deposit, northeastern Yunnan, China: Pb–Sr isotope constrains. Economic Geology 96, 583–598.
Zhou, J.P., Xu, K.Q., Hua, R.M., Zhao, Y.Y., Zhu, J.C., 1998. Characteristics and genesis of exhalative sedimentary massive sulfides in Southeastern Yunnan Province. Acta Mineralogica Sinica 18 (2), 158–168.
Zhu, C.H., Zhang, Q., Shao, S.X., Zhu, X.Q., Wang, D.P., 2008. Lead isotopic composition and lead source in the Bainiuchang Ag-polymetallic deposit, Yunnan Province, China. Acta Geologica Sinica 82 (4), 845–857.
Zhu, C.H., Liu, S.X., Zhang, Q., Gu, D.M., 2010. The exhalative-sedimentary evidence of the Bainiuchang Ag-polymetallic deposit, Yunnan, China: constraints from geochemistry of host-rocks. Geoscience 24 (1), 120–130 (in Chinese with English abstract).
Zhu, Y.Y., Han, R.S., Xue, C.D., Lu, S.L., Zou, H.J., Yuan, Z.H., 2006. Geological character of the Hetaoping Lead–Zinc deposit of Baoshan, Yunnan Province. Mineral Resources and Geology 20 (1), 32–35 (in Chinese with English abstract).